Effects of large deep-seated landslides on hillslope morphology, western Southern Alps, New Zealand

Oliver Korup[1]

Received 28 September 2004; revised 21 October 2005; accepted 12 December 2005; published 14 March 2006.

[1] Morphometric analysis and air photo interpretation highlight geomorphic imprints of large landslides (i.e., affecting ≥ 1 km^2) on hillslopes in the western Southern Alps (WSA), New Zealand. Large landslides attain kilometer-scale runout, affect >50% of total basin relief, and in 70% are slope clearing, and thus relief limiting. Landslide terrain shows lower mean local relief, relief variability, slope angles, steepness, and concavity than surrounding terrain. Measuring mean slope angle smoothes out local landslide morphology, masking any relationship between large landslides and possible threshold hillslopes. Large failures also occurred on low-gradient slopes, indicating persistent low-frequency/high-magnitude hillslope adjustment independent of fluvial bedrock incision. At the basin and hillslope scale, slope-area plots partly constrain the effects of landslides on geomorphic process regimes. Landslide imprints gradually blend with relief characteristics at orogen scale (10^2 km), while being sensitive to length scales of slope failure, topography, sampling, and digital elevation model resolution. This limits means of automated detection, and underlines the importance of local morphologic contrasts for detecting large landslides in the WSA. Landslide controls on low-order drainage include divide lowering and shifting, formation of headwater basins and hanging valleys, and stream piracy. Volumes typically mobilized, yet still stored in numerous deposits despite high denudation rates, are $>10^7$ m^3, and theoretically equal to 10^2 years of basin-wide debris production from historic shallow landslides; lack of absolute ages precludes further estimates. Deposit size and mature forest cover indicate residence times of 10^1–10^4 years. On these timescales, large landslides require further attention in landscape evolution models of tectonically active orogens.

Citation: Korup, O. (2006), Effects of large deep-seated landslides on hillslope morphology, western Southern Alps, New Zealand, *J. Geophys. Res.*, *111*, F01018, doi:10.1029/2004JF000242.

1. Introduction

[2] Mountain topography results from a complex interplay between rock uplift and surface processes. It offers sufficient relief and slope steepness for large, often catastrophic, bedrock landslides [e.g., *Abele*, 1974; *Whitehouse*, 1983; *Fort and Peulvast*, 1995; *Strom*, 1998; *Shroder*, 1998; *Hermanns and Strecker*, 1999; *Fort*, 2000; *Shang et al.*, 2003]. Research on such large landslides is generally concerned with predisposing factors, triggers, dynamics, and adverse consequences, owing to high practical demands in hazard and risk assessments. From a scientific point of view, little attention has been paid to the geomorphic significance of large landslides in general [*Densmore et al.*, 1997; *Densmore and Hovius*, 2000], and more specifically, to their role in shaping high mountain relief.

[3] Within current concepts of mountain range evolution in tectonically active settings, there are three process-based approaches to explaining relief development. First, there is a growing notion that fluvial incision in response to rock uplift sets the scale for mountain relief development [*Whipple and Tucker*, 2002; *Whipple*, 2004]. Downcutting in bedrock channels provides the ultimate base-level for slope adjustment, and thus, slope length. Assuming known regional constraints on topographic steady state, uniform uplift rates, and constant erosion rates, the so-called family of stream-power law models [*Whipple*, 2004] helps to quantify rates of rock uplift, and changes in lithology, sediment flux, or erosion from river long profiles [*Whipple and Tucker*, 2002; *Kirby et al.*, 2003; *Snyder et al.*, 2003; *Duvall et al.*, 2004]. These models provide a physically based context for empirical slope-area relationships for channels and drainage basins, and inferred fluvial and colluvial erosion laws, respectively [*Lague and Davy*, 2003]. Second, there is the view that in areas of notably high uplift, slope adjustment to fluvial incision is controlled by frequent bedrock landsliding [*Burbank et al.*, 1996]. The concept of threshold hillslopes similarly argues that rock strength limits relief through landsliding frequent enough to maintain hillslope gradients up to critical values [*Schmidt and Montgomery*, 1995; *Montgomery*, 2001]. Steeper hillslopes would thus be prone to rapid adjustment by landsliding. Third, there is growing recognition that landslides

[1]WSL Swiss Federal Institute for Snow and Avalanche Research SLF, Davos, Switzerland.

0148-0227/06/2004JF000242$09.00

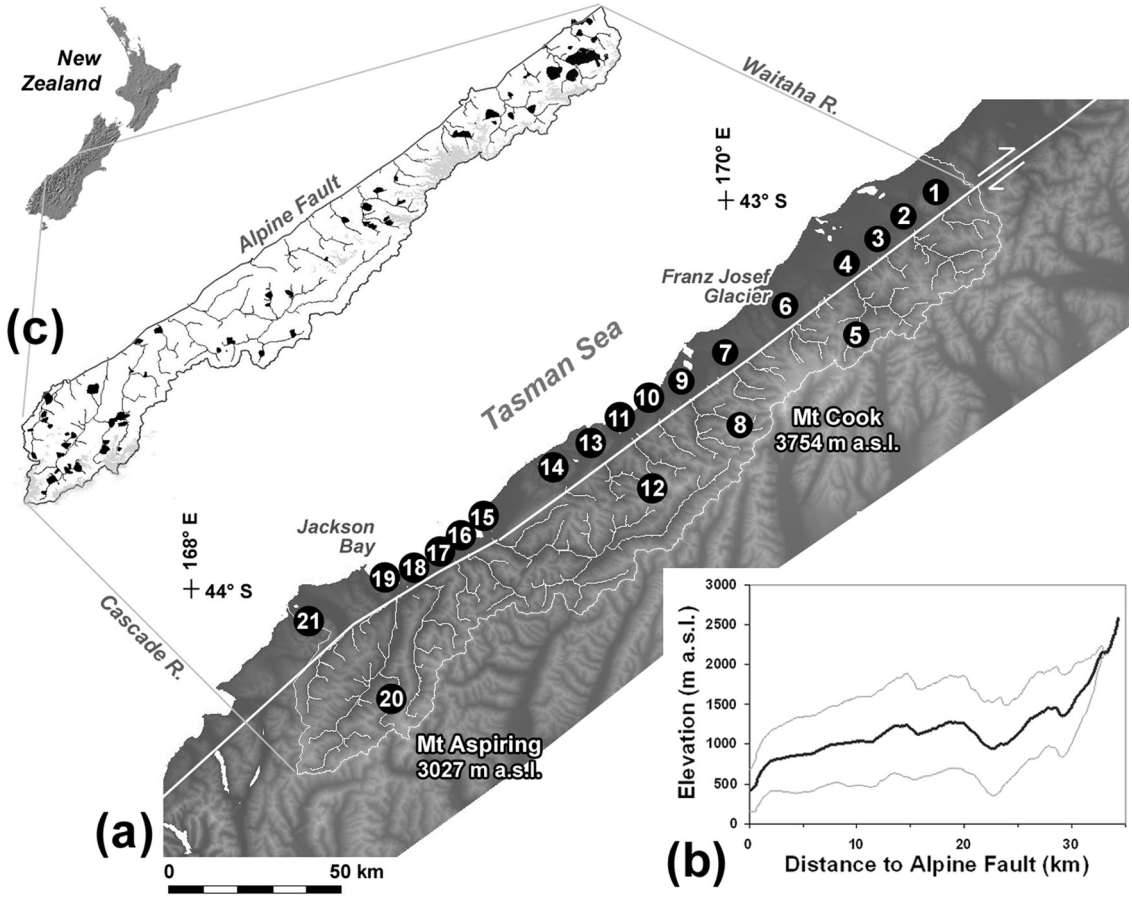

Figure 1. (a) Map of major drainage basins in the western Southern Alps (WSA), New Zealand: 1, Waitaha; 2, Wanganui; 3, Poerua; 4, Perth; 5, Whataroa; 6, Waiho/Callery; 7, Fox; 8, Copland; 9, Karangarua; 10, Makawhio; 11, Mahitahi; 12, Otoko; 13, Paringa; 14, Moeraki; 15, Haast; 16, Okuru; 17, Turnbull; 18, Waiatoto; 19, Arawhata; 20, Waipara; 21, Cascade. (b) Elevation swath profile of the WSA between the Alpine Fault and main divide; black and gray lines indicate mean and $\pm 1\sigma$ (standard deviation), respectively. Depression of mean elevation at $\sim$23 km is due to longitudinal Landsborough valley in the upper Haast basin. (c) Map of trunk river channels ($A_C > 10$ km^2) and large ($A_L \geq 1$ km^2) landslides as black areas.

are dominant erosional agents in many humid mountain belts, based on quantitative estimates of their contribution to overall sediment flux [e.g., *Hovius et al.*, 1997, 2000]. So far, this has been demonstrated for the high-frequency/low-magnitude part of the landslide spectrum, i.e., mainly shallow (<10 m thick) debris slides [*Hovius et al.*, 1997, 2000; *Martin et al.*, 2002; *Brardinoni and Church*, 2004; *Dadson et al.*, 2004]. The contribution of larger and more deep-seated (>10 m thick) landslides involving 10^6–10^{10} m^3 of rock and debris, still requires considerable attention, especially since such larger events may dominate denudation in mountain belts [*Hovius et al.*, 1997]. Despite numerous detailed site investigations, there are few regional-scale empirical studies on deep-seated bedrock landslides [*Abele*, 1974; *Whitehouse*, 1983; *Hermanns and Strecker*, 1999; *Hewitt*, 2002].

[4] This study addresses the effects of large landslides on hillslope morphology in the tectonically active western Southern Alps (WSA), New Zealand. The objectives are (1) to extend the length scale of previous regional-scale landslide studies in this area [*Hovius et al.*, 1997]; (2) to assess various methods of detecting and quantifying the geomorphic imprints of large landslides on hillslope morphology at various length scales; and (3) to discuss the implications of large landslides for relief development and adjustment, geomorphic process response, and regional sediment flux.

2. Study Area

[5] This study focuses on the westward-draining rivers of the WSA, between the Waitaha and Cascade basins (42°57′S–44°30′S, 168°16′E–170°56′E; Figure 1a). These basins bound a narrow coastal piedmont along the SW-NE striking Alpine Fault, which for 600 km marks the active dextral transpressional boundary between the Australian and Pacific continental plates. The mean plate vector of convergence is 37 mm yr^{-1} at 071° for the last 3 Myr, and the Alpine Fault accommodates 70–75% of both fault-parallel and -normal motion, attaining dip-slip rates on a

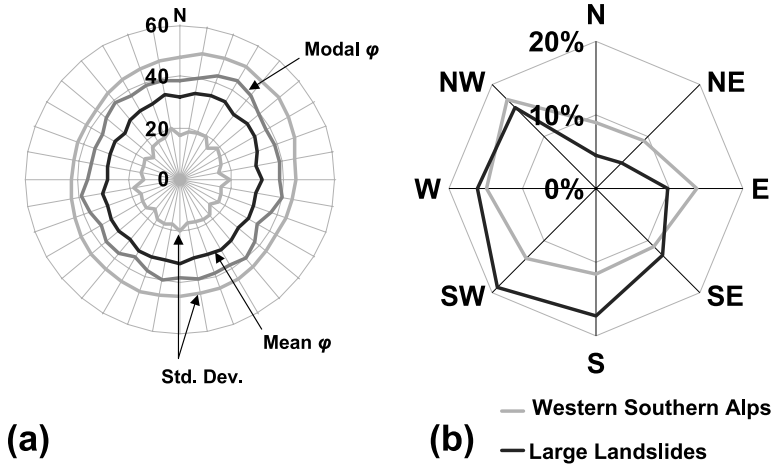

Figure 2. (a) Mean, modal, and standard deviations of slope angle φ (in degrees) (derived at 75-m length scale from a 25-m DEM) as a function of slope aspect in the WSA. Note slightly higher mean and modal φ on NE-exposed slopes. (b) Slope aspect of WSA hillslopes and landslide-affected terrain, normalized by area. Note increased density of large ($A_L \geq 1$ km^2) landslides on SW-facing slopes.

fault plane >45° between 0 and >12 mm yr^{-1} near Jackson Bay and Franz Josef, respectively [*Norris and Cooper*, 2000]. The historic (i.e., post-1850) seismic record is devoid of any high-magnitude earthquakes along the fault, but paleoseismological studies suggest $M \sim 8$ earthquakes recurring every 250–300 years on average [*Wells et al.*, 1999]. With the last event dated to 1717, there is presently a high probability for a large earthquake in the region.

[6] The WSA form the inboard of an asymmetric mountain belt, reaching a maximum elevation of 3.7 km within <20 km from the Alpine Fault (Figure 1b). Exhumed Haast Group schist of northwestward increasing metamorphic grade attains upper amphibolite facies near the Alpine Fault, while unaltered greywacke is exposed along parts of the main divide. The piedmont is made up of Ordovician basement rocks [*Norris and Cooper*, 2000] of the South Westland basin, covered by thick Cenozoic fill and Quaternary outwash from the adjacent mountain belt. The climate is mild oceanic with extreme orographically enhanced precipitation of up to 14 m yr^{-1} [*Henderson and Thompson*, 1999], resulting in high specific discharge and low annual flood variability.

[7] Several small alpine transverse catchments with a total basin relief $H_C < 3.4$ km are drained by steep and closely spaced bedrock rivers, dotted by patches of intramontane alluviation. The rivers invariably debouch onto fault-bounded alluvial fans at the mountain fringe, and flow over broad moraine-bounded alluvial plains before reaching the Tasman Sea. Much of the alpine low-order drainage is controlled by local fault, bedding, and joint patterns [*Whitehouse*, 1986; *Hanson et al.*, 1990]. Steep, rectilinear hillslopes with serrated ridges and thin regolith cover are continuously undercut and subject to frequent landsliding which, together with fluvial incision, is the dominant erosion process. Hillslopes extracted at 75-m length scale from a 25-m digital elevation model (DEM) have a modal angle $\varphi_{mod} \sim 39°$. The steepest slopes are exposed to the N, NE, and S, whereas the lowest slopes have a W–NW aspect (Figure 2a). Uplift rates appear to be roughly matched by regional denudation of <10 mm yr^{-1} [*Tippett and Kamp*, 1995]. Many traces of extensive Pleistocene glaciations were eradicated from the mountain relief, and v-shaped valley cross sections dominate. Glaciers presently cover 11% of the WSA, while ~50% of the area sustains indigenous montane rain forests up to ~1600 m a.s.l. About 90% of the forest grows on slope angles $\varphi \leq 45°$. Fluvial sediment yields approach 2.9×10^4 t km^{-2} yr^{-1}, and the regional sediment flux is 6.2×10^7 t yr^{-1} [*Hicks et al.*, 2003]. Single large historic landslides have produced short-term peaks of up to 8×10^4 t km^{-2} yr^{-1} [*Korup et al.*, 2004].

[8] Causes for landslides in the WSA are gradual reduction of rock mass strength through repeated seismic ground shaking, hanging wall rock shattering along thrust faults, and fault gouge formation [*Korup*, 2004], as well as slope oversteepening and debuttressing by deglaciation and fluvial incision. Local joint and fault intersections promote rockslide-wedge failures of schist slabs. Gravitational stress causes deep-seated failures along planes of schistosity [*Whitehouse*, 1986; *Craw et al.*, 2004], while rock-slope dilatation following unloading due to precursory landsliding also predisposes slopes to failure [*Korup and Crozier*, 2002]. Common landslide triggers are high-intensity rainstorms, fluvial undercutting, and earthquakes [*Bull and Brandon*, 1998], although several historic rock avalanches also occurred without any evident trigger [*McSaveney*, 2002].

3. Methods

[9] During a regional reconnaissance, $n = 333$ landslides (terminology follows *Cruden and Varnes* [1996]) were identified and mapped at 1:50,000 scale from over 3000 black-and-white air photos covering an area of 6056 km^2. This landslide sample is part of a larger inventory covering the montane to alpine zones of SW of New Zealand

compiled from various sources, including field checks of deposit exposures in several catchments. This study focuses on large landslides, arbitrarily defined here as those affecting a planform area $A_L \geq 1$ km^2 (including scarp and deposit). It thus complements the work of *Hovius et al.* [1997], who systematically mapped landslides in the WSA below this size.

[10] Landform assemblages diagnostic of large landslides included bare headscarps, disrupted low-order drainage, hummocky and asymmetric deposits, flow lobes, transverse furrows, distinctively uniform vegetation stands, lack of fluvial dissection, and geomorphic impacts on river channels and juxtaposed slopes [e.g., *Soeters and van Westen*, 1996]. While small debris slides and debris flows stand out as highly reflective patches in the dense forest cover [*Hovius et al.*, 1997], most large landslides in the WSA are forested. They were more efficiently detected with shaded relief and slope-angle overlays from a 25-m DEM, based on NZMS260 TopoMap 20-m contours, and subsequently verified in air-photo detail with a 2× mirror stereoscope. Photogrammetric distortion and shadow effects precluded direct mapping from air photos. Hence delineation of A_L was cross-validated with digital land cover data and contour shapes, and mapped directly onto the shaded relief. Reliability classes were assigned to the data to reflect varying mapping accuracy, while repeat digitizing tests yielded mean relative errors of ±30% for A_L, and ±15% for landslide runout L_L. Where possible, extrapolation of 20-m contours across landslide head scarps, and swath profiling of landslide surfaces, helped to approximate failure planes and pre-failure surfaces, and to estimate landslide volume V_L. The data are thus of regional reconnaissance scale and quality. Because of this uncertainty, reduced major axis (RMA) regression of log-transformed variables was used for landslide scaling relationships. The landslide density distribution was calculated following the methods of *Hovius et al.* [1997] and *Malamud et al.* [2004].

[11] There are no age or kinematic data for most of the large landslides. Mature forest covers 50% of the landslide deposits on average, indicating geomorphic surface ages >150 years. This does not warrant geomorphic inactivity, since creep movement may displace large rock masses without significantly disturbing the vegetation cover. Glacial trimming of some of the landslides indicates at least Aranuian (Holocene) age (10^3–10^4 years [*Whitehouse*, 1986]), although historic glacial advances have produced similar effects in places. Given this approximate time span covered by the inventory, it must be assumed that traces of smaller failures were eradicated from the record by subsequent larger ones.

[12] To differentiate and quantify imprints of large landslides on hillslope morphology, several geomorphometric variables were used. The underlying hypothesis is that any geomorphic imprints should show in the distributions of these variables, sampled across individual and total landslide-affected terrain A_L, and A_{LT}, respectively, which are expected to differ from those of unaffected areas. Given that $L_L \sim A_L^{0.5}$ [*Korup*, 2005b], it is expected that local morphologic imprints of large landslides should show at a sampling radius $R < 1$ km. To obtain a measure of typical length scales in the WSA, hillslope length was calculated as the plan distance from catchment divides to major river channels, arbitrarily defined here as drainage lines with a contributing catchment area $A_C \geq 10$ km^2 to exclude the effect of headwater basins. The resulting average slope length is 1.5–2.4 km for any of the basins in Figure 1. Since the maximum divide half-spacing is ~4.5 km, values of $R > 4.5$ km would include unwanted relief properties of adjacent drainage basins.

[13] Terrain variables extracted from the 25-m DEM were elevation E, slope angle φ, as well as profile and plan curvature. Mean local relief H_R and relief variability SD_R were calculated as the maximum difference, and standard deviation, of E within a moving circle window of radius R, respectively. The same neighborhood approach was used to measure standard deviation of local slope SD_φ, as an indicator of roughness. These simple measures were preferred to more sophisticated approaches [e.g., *Aharonson et al.*, 2001; *McKean and Roering*, 2004] in view of the landslide mapping accuracy, and the DEM data source, which derived from air photos in densely forested terrain, contains an unknown degree of roughness due to canopy effects. Furthermore, the Gaussian shape of histograms of E and φ over various sampling areas justifies the use of standard deviation-based neighborhood statistics for this first-order regional approach.

[14] Local gradient S and A_C were obtained for large landslides and randomly placed and presumably unaffected sample areas surrounding the landslides. Bins of $\log(A_C)$ were used to avoid bias due to the higher number of data points for smaller values of A_C [*Lague and Davy*, 2003]. The steepness index k_s and concavity index θ [*Sklar and Dietrich*, 1998] were obtained from RMA regression of S and A_C from log-binned data, based on the empirical relationship

$$S = k_s A_C^{-\theta}. \tag{1}$$

Significant breaks between scaling regimes helped to define the transition between hillslope and fluvial channels. Here, k_s and θ solely serve as morphometric indices to measure the effect of large landslides on hillslope morphology, without addressing any potential implications on rates of rock uplift and erosion, lithology, process types or sediment supply [*Sklar and Dietrich*, 1998]. Since k_s has units of km$^{2\theta}$, A_C was normalized by a reference area A_r,

$$S = S_r (A_C / A_r)^{-\theta}. \tag{2}$$

The reference slope S_r allows comparison of steepness values between various basins, and reduces covariance between k_s and θ [*Sklar and Dietrich*, 1998]. In addition, k_{s*} was averaged from the same log bins for an arbitrarily fixed reference θ_r [*Kirby et al.*, 2003], determined by the concavity of the sample area surrounding the landslide. The stream power index

$$SPI = A_C S \tag{3}$$

defined by *Moore et al.* [1993] was also extracted for both hillslope and channel cells. The SPI is also used here as a relief indicator of erosion potential, and not a means to

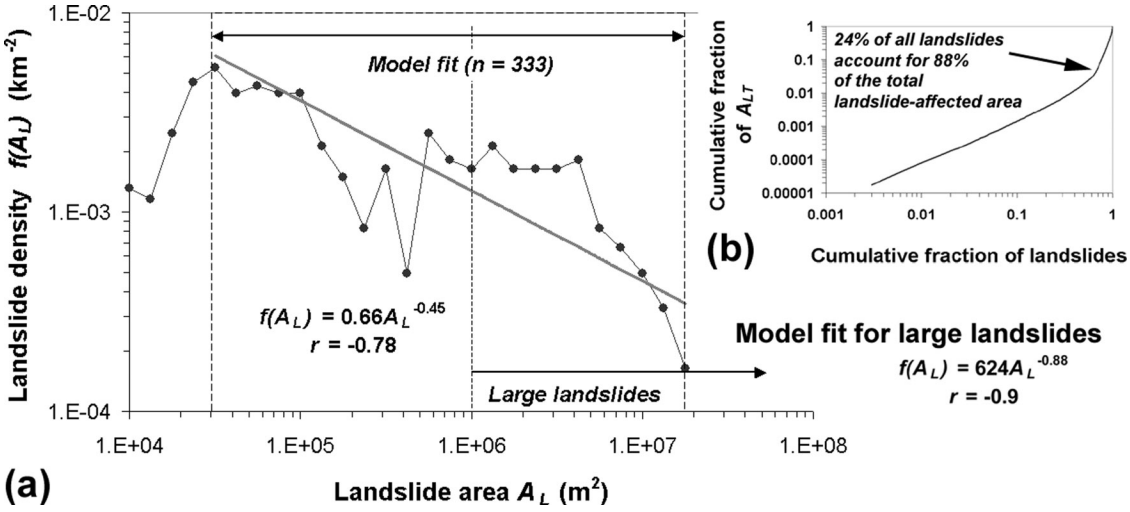

Figure 3. (a) Landslide density distribution $f(A_L)$ (histogram) of n = 333 landslides in the WSA, using logarithmic bin width normalized by landslide area A_L. (b) Cumulative increase of fraction of landslide-affected area A_L as a function of percentage of total landslide occurrences.

accurately model local stream erosion [*Finlayson and Montgomery*, 2003].

4. Large Landslides and Hillslope Morphology

4.1. Size Distribution and Characteristics

[15] The density distribution of a sample of n = 333 landslides $f(A_L)$ in the WSA roughly shows a inverse power law trend over nearly three orders of magnitude (3×10^4 m$^2 \leq A_L < 2 \times 10^7$ m^2), with a slope $\beta = 0.45 \pm 0.06$ ($r = -0.78$, Figure 3a). Given that $\beta < 1$, the larger landslides dominate this distribution by area. At least 80 such large landslides of various types affect a total area of 275 km^2. While making up 24% of the data, they constitute 88% of the total landslide-affected area A_{LT} = 313 km^2 (Figures 1c and 3b). The density distribution of large landslides has a higher slope $\beta = 0.88 \pm 0.11$ ($r = -0.9$), though the small number of data points precludes any robust fit. Most of the large landslides have estimated deposit volumes $V_L = 10^7$–10^8 m^3 (Table 1). The scaling relationship between landslide volume V_L (km^3) and A_L (km^2),

$$V_L = \varepsilon A_L^b, \tag{4}$$

where $0.01 \leq \varepsilon < 0.05$, and $1.30 \leq b < 2.56$, is derived from landslide data compiled from various mountain belts (Table 2). Despite the circular argument that V_L is commonly calculated by multiplying A_L with an average deposit or failure thickness, ε and b show remarkable consistency for a variety of landslide types, size ranges, calculation methods,

Table 1. Selected Large and Deep-Seated Landslides in the Western Southern Alps[a]

N	Location	Catchment	Type	Lithology[b]	A_L, km^2	V_L, Mm^3	H_L, km	H_L/H_C	H_L/H_S	L_L, km	φ_{mod}, deg	Failure Plane γ, deg	Notes[c]	NZ Map Grid
1	Ruera	Copland	slide/flow	G-O	2.4	n.c.	1.4	0.46	1	3.1	22	n.c.		2267300E 5726770N
2	Jumbo Ck	Makawhio	rock flow[d]	G-O	3.5	240	1.3	0.55	1	2.8	30	16–36	OC	2248330E 5270770N
3	Selbourne Spur	Waiatoto	rock avalanche	G-O, ?FR	3.4	90	0.8	0.27	1	3.3	7	n.c.	P	2177980E 5679570N
4	Macfarlane	Haast	rock flow	n.c.	3.8	310	1.3	0.48	1	2.4	39	38	OC	2222250E 5695100N
5	Misty Peak	Karangarua	complex rotational slide[d]	B	6.7	800	1.5	0.48	1	3.2	23	19–35		2255680E 5725290N
6	Urquart Knob	Waitaha	block slide	G-O	3.0	335	1.0	0.40	1	2.2	38	28	F	2327980E 5784600N
7	Climax Spur	Burke	rock flow	n.c.	3.2	300	1.1	0.40	1	2.1	27	44	F	2208980E 5679600N
8	Bealy Range	Haast	rock flow	n.c.	3.4	n.c.	1.2	0.44	1	2.5	25	n.c.	RR	2230480E 5682230N
9	Princes Ck	Okuru	slide	B/G-O	1.9	n.c.	1.0	0.51	0.78	1.7	30	n.c.	OC	2205320E 5676480N
10	Hyperia	Waiatoto	rotational slide[d]	G-O	6.0	550	1.6	0.53	1	2.7	38	23		2171760E 5654050N
11	Hyperia NE	Waiatoto	rotational slide	G-O	1.0	>27	0.8	0.27	0.5	1.3	31	34	SF	2172160E 5654400N
12	Cheyenne Ck	Haast	rotational slide	G-O	1.4	n.c.	1.0	0.37	0.62	1.7	29	n.c.		2221900E 5691910N
13	MacArthur's Flat	Arawhata	slide	G-O	1.5	40	1.3	0.43	1	2.1	36	36	FRD	2150230E 5635410N
14	Falls Ck	Cascade	rotational slide[d]	U	2.1	130	0.8	0.42	0.8	2.3	38	n.c.	F, FRD	2146100E 5652740N

[a]"Not calculated" denoted by n.c.
[b]Haast Schist facies: B, biotite; G-O, garnet-oligoclase; FR, schist-derived fault rock; U, ultramafics.
[c]F, fault-controlled; FRD, former rockslide dam; OC, channel occlusion, i.e., partial blockage or diversion of channel; P, runout onto piedmont; RR, ridge rents; SF, secondary failure.
[d]Includes multiple (secondary) failures.

Table 2. Scaling Relationships Between Landslide Volume V_L and Area A_L (Irrespective of Landslide Type) Derived by Reduced Major Axis Regression From Log-Transformed Data[a]

Region	Minimum A_L, km^2	ε	b	r	n	Key Reference
Western Southern Alps	0.005	0.05 ± 0.02	1.50	n/a	4984	*Hovius et al.* [1997]
Central Southern Alps	0.05	0.03 ± 0.01	1.54 ± 0.14	0.78	45	*Whitehouse* [1983]
Central Southern Alps	1	0.01 ± 0.008	2.56 ± 0.69	0.65	8	*Whitehouse* [1983]
European Alps	0.02	0.02 ± 0.003	1.62 ± 0.09	0.91	63	*Abele* [1974]
European Alps	1	0.03 ± 0.006	1.42 ± 0.15	0.74	43	*Abele* [1974]
High Asia	1	0.02 ± 0.01	1.30 ± 0.18	0.65	29	*Hewitt* [2002]
SW New Zealand	0.2	0.01 ± 0.002	2.45 ± 0.17	0.92	34	this study
SW New Zealand	1	0.02 ± 0.003	1.95 ± 0.13	0.95	23	this study
Pooled Mean	0.05	0.02 ± 0.002	1.55 ± 0.05	0.89	171	this study
Pooled Mean	1	0.03 ± 0.005	1.38 ± 0.09	0.77	94	this study

[a] V_L in km^3; A_L in km^2. Scaling relationship is $V_L = \varepsilon A_L{}^b$. Coefficients include ±1σ (standard deviation) and correlation coefficient r.

and study areas. Equation (4) suggests that, allowing for discrepancy between scar and deposit volumes due to debris dilatation, the largest landslides in the WSA would mobilize $V_L \sim 10^{10}$ m^3, matching well with earlier size estimates of such "mountain-slides" [*Whitehouse*, 1986]. With $b > 0$, equation (4) also indicates that large landslides may also dominate the total mobilized volume. Whether this also applies to sediment production rates cannot be determined without better age constraints on the large landslides in particular.

[16] The mean thickness of large landslides, $V_L\ A_L^{-1}$, ranges between 1 and 120 m, with an average of 46 m (n = 20). Most of them are deep-seated bedrock failures, and *Whitehouse* [1986] noted that some of them mobilized >100-m-thick slabs of schist. No large landslides were observed to initiate above 2200 m a.s.l. owing to limits in ridge heights and extensive glacier cover. The height of individual landslides H_L extends over 40–50% of total basin relief H_C, and >50% of local slope relief H_S, measured from the divide to the trunk channel (Table 1). Some 70% of the detected large landslides are slope-clearing features [*Densmore et al.*, 1997], for which $H_L \geq H_S$.

[17] Spatial density of large landslides in the WSA is 1.2×10^{-2} km^{-2}, i.e., 3 times that of rock avalanches in the central Southern Alps (4.2×10^{-3} km^{-2} [*Whitehouse*, 1983]), and that of large deep-seated failures in the stronger crystalline basement rocks of the adjacent Fiordland Mountains (4×10^{-3} km^{-2} [*Korup*, 2005b]). In the WSA, large landslides affect between 1–20% of total basin area in the major catchments ($A_C > 60$ km^2), although this percentage is largely independent from A_C. Drainage density on landslide-affected terrain is lower by 10–20% for high-order streams (A_C = 10, and 1 km^2, respectively). However, there is no significant difference for channels with A_C = 0.1 km^2, which in the WSA are mostly steep gullies associated with shallow landslides and debris flows. Large-scale slope instability shows a strong spatial coincidence with structural controls. Some 75% of the area affected by large landslides is within 1 km of geological lineaments, and 60% of the landslides intersect with lineaments >0.1 km in length. These structures include secondary faults, joints, and "ridge rents," i.e., counter- or uphill-facing scarps [*Beck*, 1968]. The average length density of lineaments per large landslide is 7.2 km km^{-2}.

4.2. Geomorphometric Analysis

[18] In the following, geomorphometric analysis is used to test whether the geomorphic imprint of large landslides on hillslope morphology can be quantified by the shape and characteristics of histograms of various morphometric variables. Terrain affected by large landslides generally occupies a lower elevation range with a mode ~400 m lower than that in the WSA (Figure 4a and Table 3). Elevation histograms show a slightly skewed Gaussian distribution, which appears to be compressed for landslide-affected terrain. This pattern is also evident at the basin scale (10^1 km), although the difference between modes is less prominent (Figure 4b). In terms of mean local relief H_R, and relief variability SD_R, landslide terrain shows negative deviations from the regional means, modes, and maxima, which for SD_R

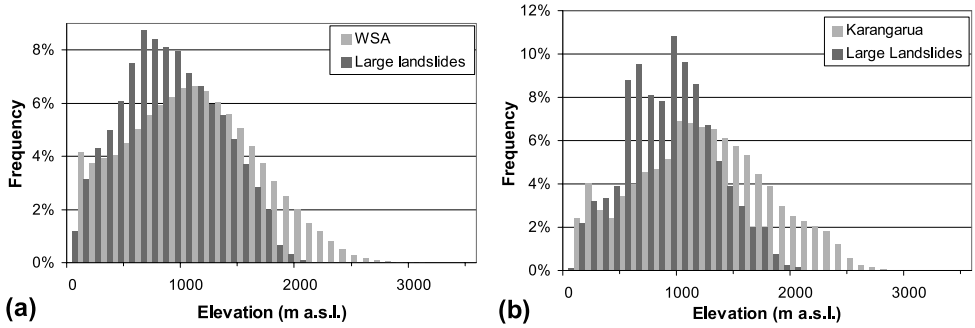

Figure 4. Area-normalized elevation histograms for the (a) WSA and (b) Karangarua basin (location 9, Figure 1a), and terrain affected by large ($A_L \geq 1$ km^2) landslides.

Table 3. Geomorphometric Variables for the Western Southern Alps and Terrain Affected by Large ($A_L \geq 1$ km^2) Landslides, Derived From Area-Normalized Histograms at 25-m Grid Resolution[a]

Variable	Mean/Mode/Maximum	WSA	Large Landslides
E, MASL	mean	1023 ± 564	899 ± 429
	mode	1050	650
	maximum	3488	2159
SD_R, m (R = 125 m)	mean	39 ± 20	36 ± 14
	mode	35	35
	maximum	218	138
SD_R, m (R = 250 m)	mean	71 ± 32	65 ± 22
	mode	75	65
	maximum	283	128
SD_R, m (R = 500 m)	mean	124 ± 51	116 ± 36
	mode	125	125
	maximum	395	268
SD_R, m (R = 1000 m)	mean	200 ± 76	199 ± 58
	mode	205	195
	maximum	527	403
H_R, m (R = 250 m)	mean	198 ± 161	268 ± 89
	mode	290	270
	maximum	1002	681
φ, deg	mean	31 ± 14	30 ± 12
	mode	39	30
	maximum	82	76
SPI	mean	1.3 ± 0.6	1.3 ± 0.6
	mode	1.4	1.1
	maximum	6.3	4.3

[a] E, elevation; SD_R, relief variability (i.e., standard deviation of elevation); H_R, mean local relief; φ, slope angle; *SPI*, stream power index [*Moore et al.*, 1993]; MASL, meters above sea level. Mean values are listed with ±1σ (standard deviation).

are most pronounced for lower values of R (Figure 5 and Table 3). The higher mean of H_R for landslide-affected terrain with respect to the study area derives from the additional smoothing effect of low-gradient valley floors in the WSA histogram (Table 3). Similar characteristics of reduced relief variability SD_R and mean local relief H_R of landslide-affected terrain are evident at basin scale, where increasing R leads to a pronounced bimodality in SD_R (Figure 5). Increasing R also reduces the relatively lower standard deviation of local slope SD_φ of landslide terrain (Figures 6 and 7).

[19] Comparison of slope histograms illustrates the generally lower hillslope angles in landslide terrain (Figure 8a). Despite similar mean slopes Φ, modal slope φ_{mod} of A_{LT} negatively deviates by 20% from that of the WSA (Table 3), an effect also evident at the basin scale (Figure 8b). Locally, however, φ_{mod} of large landslides with low displacement of rock masses is not discernible from that of the region (Table 1). Plots of φ in landslide-affected terrain, as a function of elevation, mirror regional trends, although they appear compressed along their x axis (Figure 9). For a given elevation, large landslides tend to produce higher minimum and lower maximum values of φ. This smoothing effect on the range and standard deviation of φ is most prominent at ∼2000 ± 150 m a.s.l., i.e., near the observed upper elevation band of large landslides (Figure 9). Most importantly, large landslides do not significantly alter mean slope angles Φ across all elevation bands (Figure 9c). Differences in histograms of plan or profile curvature between landslide terrain and the WSA are statistically insignificant. Most of the large landslides have a SW aspect (Figure 2b), and very few large failures were detected on NE-facing slopes, which also are ∼5° steeper on average than those of a SW aspect.

[20] Mean values of SPI are insensitive to the slope-lowering effect of large landslides, although modal values may be reduced by up to ∼20% (Table 3). Terrain affected by large landslides tends to have a lower concavity index θ than that of a randomly placed surrounding area (Figure 10). Generally, landslides produce lower gradients near divides, but higher gradients on mid- and toe slopes upstream of fluvial channelization (Figure 10). For selected landslides (Figure 10), k_{s*} is 0.4–12.3% lower than in unaffected surrounding areas. Differences in values of S_r between landslide and unaffected terrain remain within 1σ, and hence have little indication potential.

4.3. Failure Types and Influence on Hillslope Morphology

[21] The quantitative analysis of large landslides on hillslope morphology was augmented by air photo interpretation (API) and field checks. This qualitative approach adds more detail on geomorphic process response not evident from geomorphometry. Most of the large landslides mapped are deep-seated complex rotational or translational failures [*Cruden and Varnes*, 1996], which have created distinct amphitheater-shaped scars, locally extending to ridge crests (Figure 11). Their deposits are typically subdued and hummocky, comprising disrupted rock blocks and local flow lobes. Few catastrophic rock avalanches have fallen from the range front and ran out onto the piedmont, where their deposits are partly preserved [*Korup*, 2004]. Their detachment caused local catchment initiation (10^{-1} to 10^{0} km^2), enlargement, and relief inversion [*Blair*, 1999; *Hovius et al.*, 1998; *Korup*, 2004].

[22] About 70% of the large landslides appear to be either presently inactive or extremely slow moving. API shows well-developed multiple tension cracks, lateral scarps along plunging ridge lines, differential slope deformation, and bulging mid- to toe-slopes indicating partly detached rock masses. Similar to shallow (∼10 m) landslides, such failures leave barely detectable imprints with respect to the regional slope distribution (Figures 12b and 12f). In contrast, catastrophic failures with long runout cause the most significant changes to local slope distributions, followed by complex rotational rock slides (Figures 12a, 12c, and 12d). Many of the deep-seated failures are controlled by dip-slope schistosity or planes of structural weakness, and have created rectilinear hillslopes (Figure 12e) [*Whitehouse*, 1986; *Craw et al.*, 2004; *Korup*, 2005a].

[23] The largest landslides involve rock flow or deep-seated gravitational slope deformation (DSGSD) [*Chigira*, 1992; *Agliardi et al.*, 2001], and possible lateral spreading with $A_L \sim 10^1$ km^2. Key diagnostic landforms include kilometer-scale ridge rents [*Beck*, 1968], ridge-crest spreading, and dense spacing of interfluves. Some DSGSD show intense brittle surface deformation with high density of fault traces, and shape the hummocky or chaotic surface of whole valley sides. In the Smyth and Lord Ranges, Wanganui River (location 2, Figures 1a and 13), they involve rotated and dislodged rock blocks, terracettes, micro-grabens, tensional depressions filled by ponds, and bulging mid and toe slopes [*Korup*, 2005a]. A well-defined ridge rent, which appears to be part of a set of E-trending lineaments,

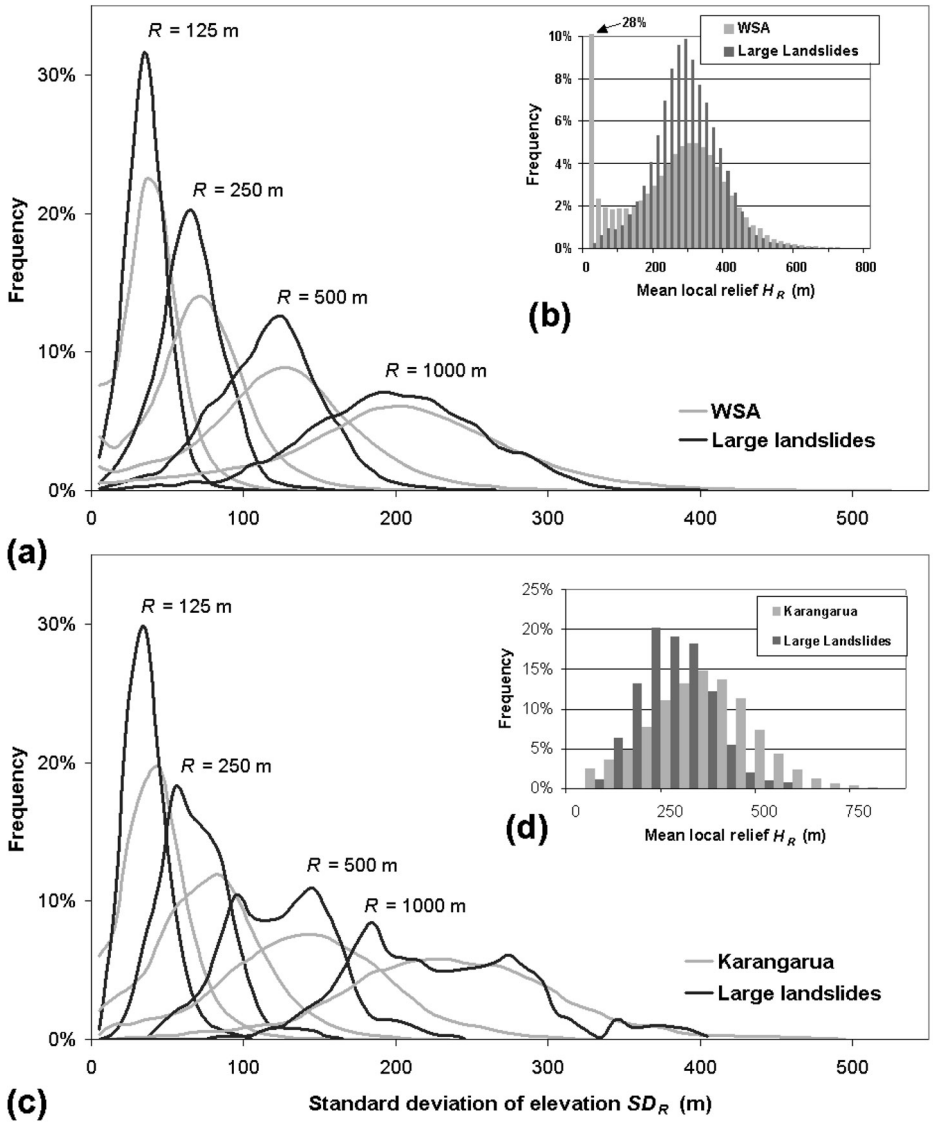

Figure 5. Smoothed histograms of relief variability SD_R, i.e., standard deviation of elevation within radius R normalized by area for (a) the WSA and (c) Karangarua basin (location 9, Figure 1a), and terrain affected by large ($A_L \geq 1$ km^2) landslides. Note growing similarity of SD_R with increasing R. (b, d) Histograms of mean local relief H_R, calculated as the maximum elevation difference within R = 250 m.

truncates the slopes below the Lord Range near Devastation Creek. It strikes 78°E toward Camp Saddle (CS, Figure 14), and its tentative extension forms a gully sidewall in Benighted Creek further downstream along the main valley (BCk, Figure 13). The ridge rent created a straight and 2.6-km-long hanging valley of asymmetric cross section, with an average depth of ~100 m, that drains subparallel to the main valley. The valley floor is infilled with snow avalanche/rockfall/debris flow cones from the Lord Range (C, Figure 14). The local strike of schist foliation in the rock-walled gully of Devastation Creek is ~75°E, estimated from API, and bulging foliation follows the local contours. Asymmetric valley cross sections illustrate the effects of DSGSD-induced slope bulging (Figure 14), which may gradually divert river channels. In other locations, this has led to fluvial undercutting of juxtaposed toe slopes and upslope propagation of concave erosional fronts of secondary retrogressive landsliding and pronounced gully erosion. In the upper Arawhata River, for instance, channel diversion caused by the Mercer landslide (A_L ~8.5 km^2) led to such vis-à-vis effects over an area of 5.2 km^2.

[24] API also revealed ridge and divide migration, where portions of the crest were entrained into the failing landslide mass. A good example is located in the Karangarua basin, where 7% of the drainage basin area (A_C = 361 km^2) is affected by at least eight large landslides (location 9, Figure 1a). One of these, a complex rotational rockslide (A_L = 6.7 km^2, V_L ~800 × 10^6 m^3) in biotite schist below Misty Peak in the Karangarua Range, caused truncation of headwater streams and catchment enlargement by ~0.4 km^2 at the headscarp (Figure 15). The former divide below the headscarp was lowered vertically by ~0.25 km, i.e., ~20%

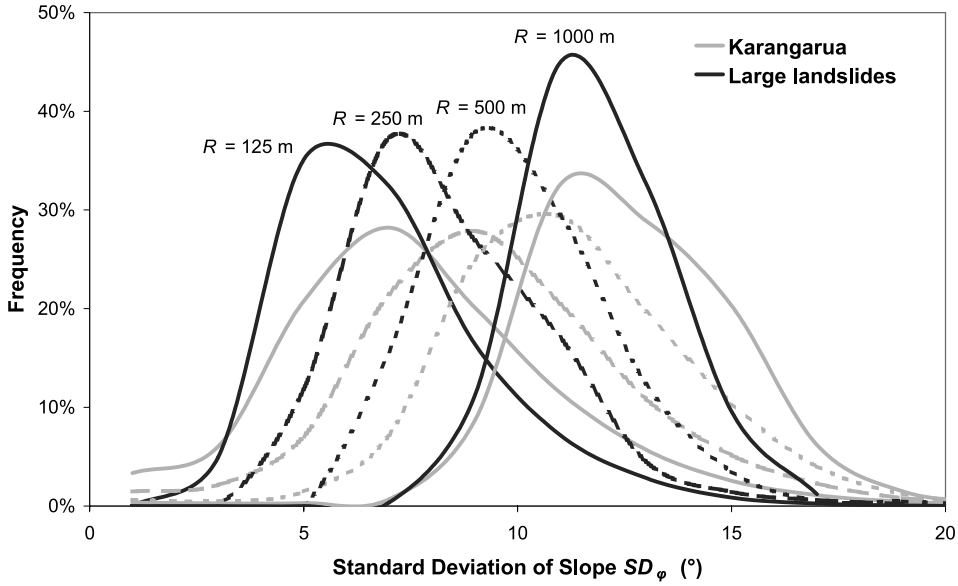

Figure 6. Smoothed histograms of standard deviation of local slope SD_φ within radius R, normalized by area for the Karangarua basin, and terrain affected by large ($A_L \geq 1$ km^2) landslides. Stippling differentiates curves for varying R.

of the total slope relief H_S = 1.2 km. The maximum headward divide retreat is estimated at ~0.5 km. This has shortened the local divide spacing in adjacent Regina Creek by ~20%. This equals to 8% of the regional maximum divide half-spacing, while the landslide-induced divide retreat reduced the basin area of Regina Creek by 2.5%. A large (A_L = 2.1 km^2, V_L ~130 × 10^6 m^3) rotational rock slide at Falls Creek, Cascade River (location 21, Figure 1a), caused similar divide retreat and lowering of <0.2 km, and 0.1 km, respectively (Figure 11). Many other ridge crests in the WSA, including the main divide, show numerous erosional scarps truncating low-order channels, possibly

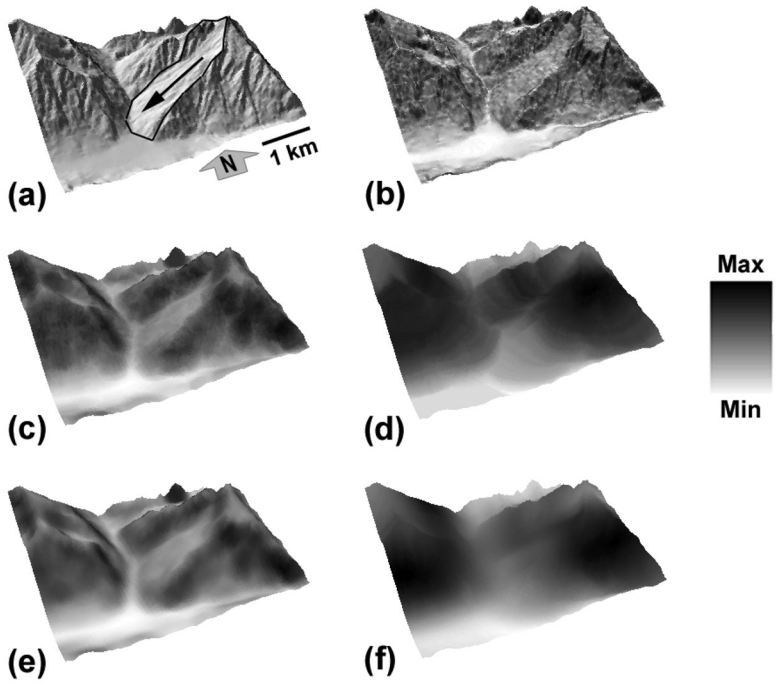

Figure 7. Smoothing effect of Ruera landslide on local hillslope morphology, Copland River (location 8, Figure 1a, and Table 1). (a) Shaded relief image with landslide outline and direction of movement (thin black arrow). (b) Slope angles φ. (c) Mean local relief H_R for R = 250 m. (d) H_R for R = 1000 m. (e) Standard deviation of elevation SD_R for R = 250 m. (f) SD_R for R = 1000 m (all data derived from 25-m DEM). Shading key applies to Figures 7b–7f.

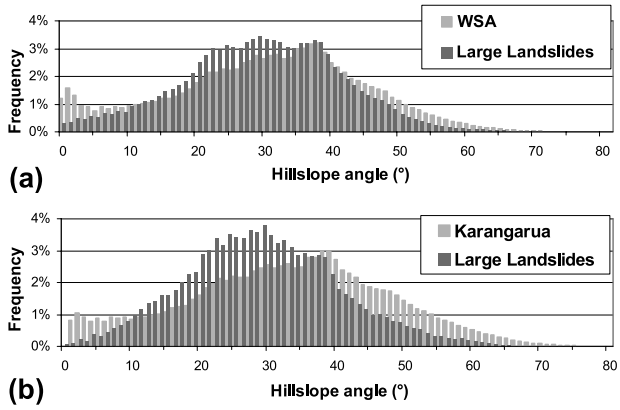

Figure 8. Area-normalized hillslope angle histograms for (a) the WSA and (b) Karangarua basin (location 9, Figure 1a), and terrain affected by large ($A_L \geq 1$ km^2) landslides.

indicating former detachment of deep-seated landslides [*McSaveney*, 2002].

5. Discussion

5.1. Landslide-Induced Changes to Hillslope Relief

[25] The data on large landslides in the WSA presented here are the results from a regional reconnaissance study, and open to future refinement. The regional landslide magnitude-frequency distribution appears to be dominated by large events, although the low number of large landslides does not warrant a very robust fit (Figure 3). Ideally, the dataset would need to see combination with that of *Hovius et al.* [1997]. However, (1) the lack of absolute ages, (2) possible reactivations, and (3) potential chronic slope deformation at some of the sites rule out this option. However, the observed scale invariance is surprising given that no age data are available for the larger failures [*Korup*, 2005c]. Large landslides are important relief-limiting agents, since most of them affect the full local slope relief ($H_L \geq H_S$). Geomorphometric analysis at comparable length scales shows that large landslides dampen local relief, removing mass from upper slopes and depositing debris on lower slopes, thereby shifting peaks in elevation histograms below the regional mode (Figure 4). Large landslides further promote lowering in mean local relief H_R, relief variability SD_R, slope angle φ, and standard deviation of local slope SD_φ at basin- and, to a lesser degree, orogen-scale (Table 3 and Figure 7). This effect is more evident for modal than for mean slopes (Table 3 and Figures 8 and 9c). Mean slope angle Φ is an insensitive measure here, since it smoothes the local variation of steeper landslide detachment areas and lower slope angles on the subdued deposit surface. Modes of φ may thus better characterize hillslopes in the WSA, while failure type and runout are important local controls otherwise subsumed in histogram data (Figure 12). Large landslides also lower basin-wide steepness and concavity, k_{s*} and θ (Figure 10). The amount of these changes depends, however, on how large A_L is relative to the surrounding "reference area." Also, the possible effects of other, undetected, landslides in these surrounding areas may not be fully accounted for. Lower gradients in headwaters and slightly higher gradients on lower hillslopes are likely the result of (1) slope adjustment in detachment areas near divides, (2) hummocky debris deposits on mid and toe

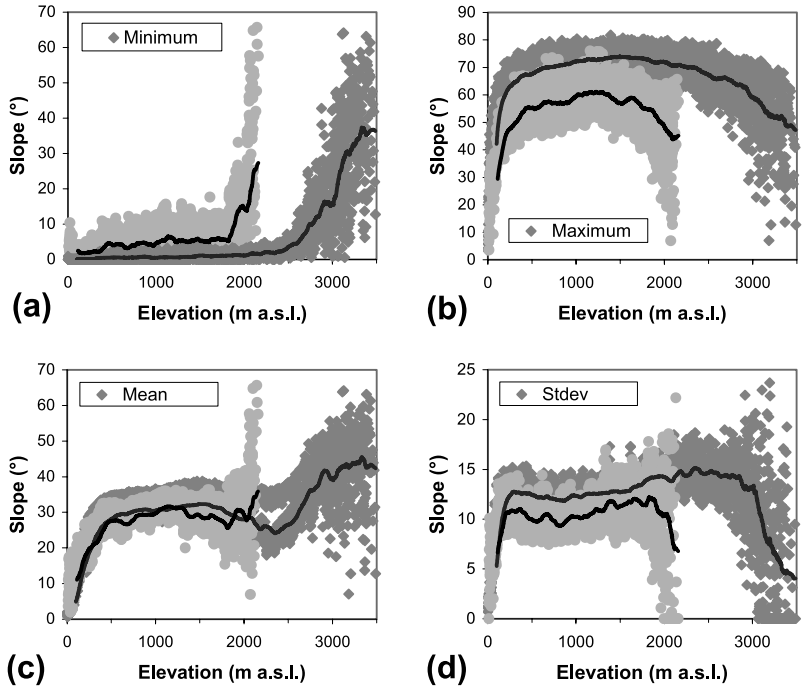

Figure 9. Hillslope angle φ as a function of elevation for the WSA (dark gray dots) and large ($A_L \geq 1$ km^2) landslides (light gray dots), all sampled at 25-m resolution (i.e., at 75-m length scale). (a) Minimum, (b) maximum, (c) mean, and (d) standard deviation of φ. Black lines indicate running mean (100-m period). Note that deviation is least pronounced for mean slope angles.

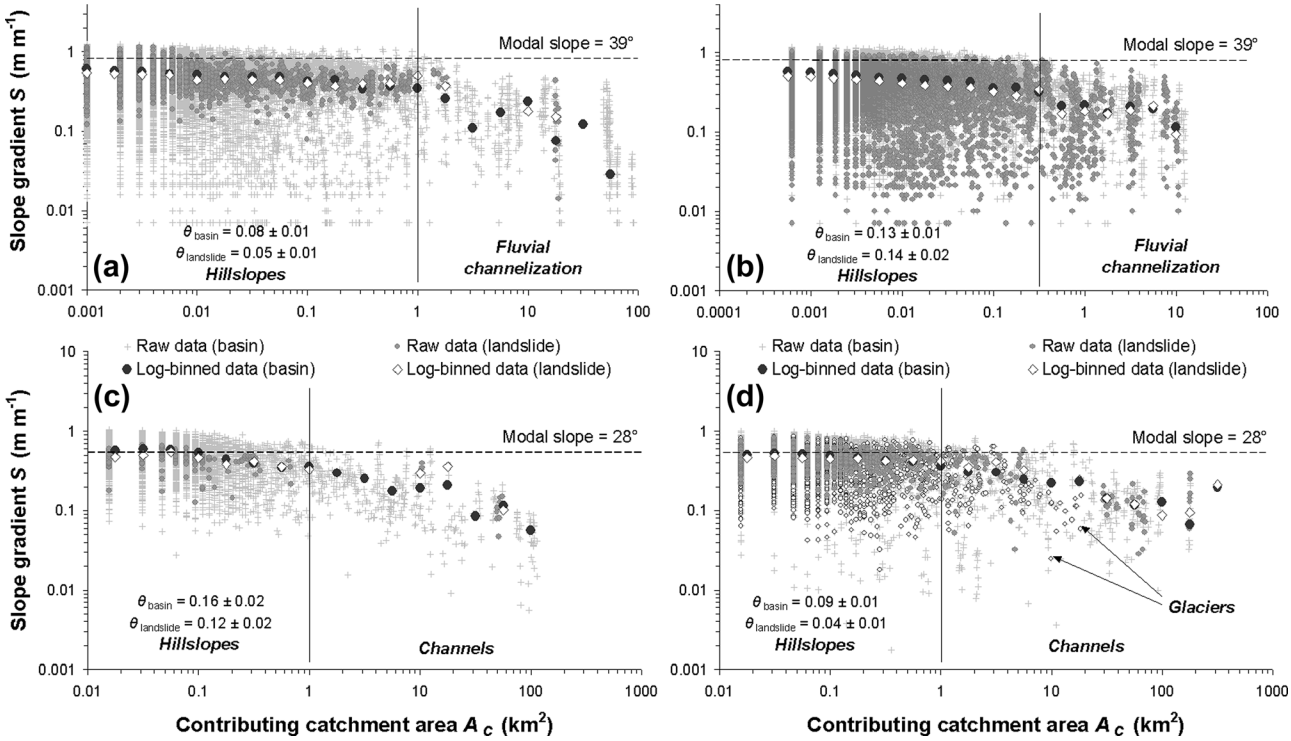

Figure 10. Slope-area plots for drainage basins and areas affected by large ($A_L \geq 1$ km^2) landslides in the WSA. Raw data were log-binned to avoid bias of high number of data points for small values of A_C. (a) Ruera landslide (A_L = 2.4 km^2), and area of 5 km × 5 km randomly placed around landslide, Karangarua basin. (b) Thomson Range collapse ($A_L \sim$ 11 km^2), and area of 6 km × 6 km randomly placed around landslide, Arawhata basin. (c) Jumbo Creek rockslide-rock flow (A_L = 3.5 km^2), and Makawhio catchment (A_C = 114 km^2). (d) Eight landslides (total $A_L \sim$ 24 km^2) and upper Joe/Arawhata River basin (A_C = 180 km^2). Data were derived from a 25-m DEM (Figures 10a and 10b), and a resampled 125-m DEM (Figures 10c and 10d), hence the differences in regional modal slope. Concavity index $\theta \pm 1\sigma$ was derived from RMA regression with best-fit power law model $S = k_s A_C^{-\theta}$. See text for explanation.

slopes, and (3) shallow landslide- and debris flow–dominated gully incision into large landslide bodies. Values of log-binned k_{s*} for landslide terrain steadily increase toward the fluvial channelization threshold, supporting the notion of pronounced debris-flow incision.

[26] The similarity of histograms limits use of H_R, SD_R, SD_φ, and φ for automated detection of large landslides for both R = 1 km and at orogen scale (10^2 km). Although the quantitative deviation between histograms is dependent on the choice of R and DEM resolution [*Finlayson and Montgomery*, 2003], local contrasts are more important. The detection of such local contrasts in surface roughness, however, also depends, apart from R, on the choice of an appropriate surrounding area undisturbed by large landslides. In some parts of the WSA, significant portions of valley walls are subject to deep-seated failure [*Craw et al.*, 2004], and hence may not yield conclusive evidence for low values of R. Using compound morphometric variables and topographic vis-à-vis effects aids the detecting of large landslides. *McKean and Roering* [2004] stated that statistical details of roughness measures were less important than appropriate grid resolution and sampling length scales. Using high-resolution (i.e., 1.5–10 m) laser altimetry data, they observed a significantly higher topographic roughness of a large earthflow with respect to adjacent unforested soil-mantled terrain in New Zealand hill country. For R = 250 m, for example, large landslides in the WSA may also be smoother and less dissected than adjacent terrain (Figure 7). In most cases, the scope for better linking landslide morphology to failure process mechanics in the WSA needs to overcome the problem of reliably differentiating key causes and triggers of large-scale slope instability.

[27] API of large landslides matches model observations, in which deep-seated rotational slides create distinctively concave headscarps on upper slopes [*Densmore et al.*, 1997]. Together with detectable changes in hillslope morphometry, API supports the notion that geomorphic imprints of large slope-clearing failures (Figures 11 and 15), though less numerous than smaller events (Figure 3), may be more persistent. This is because large landslides are deeper, and change the attributes of the topography, whereas smaller landslides do not appear to do so: Instead, they simply lower the topography. Landslide-driven relief limitation is evident in numerous erosional scars that truncated headwater basins and caused divide retreat. Such divide migration exerts a first-order control on local ridge-crest relief, drainage basin

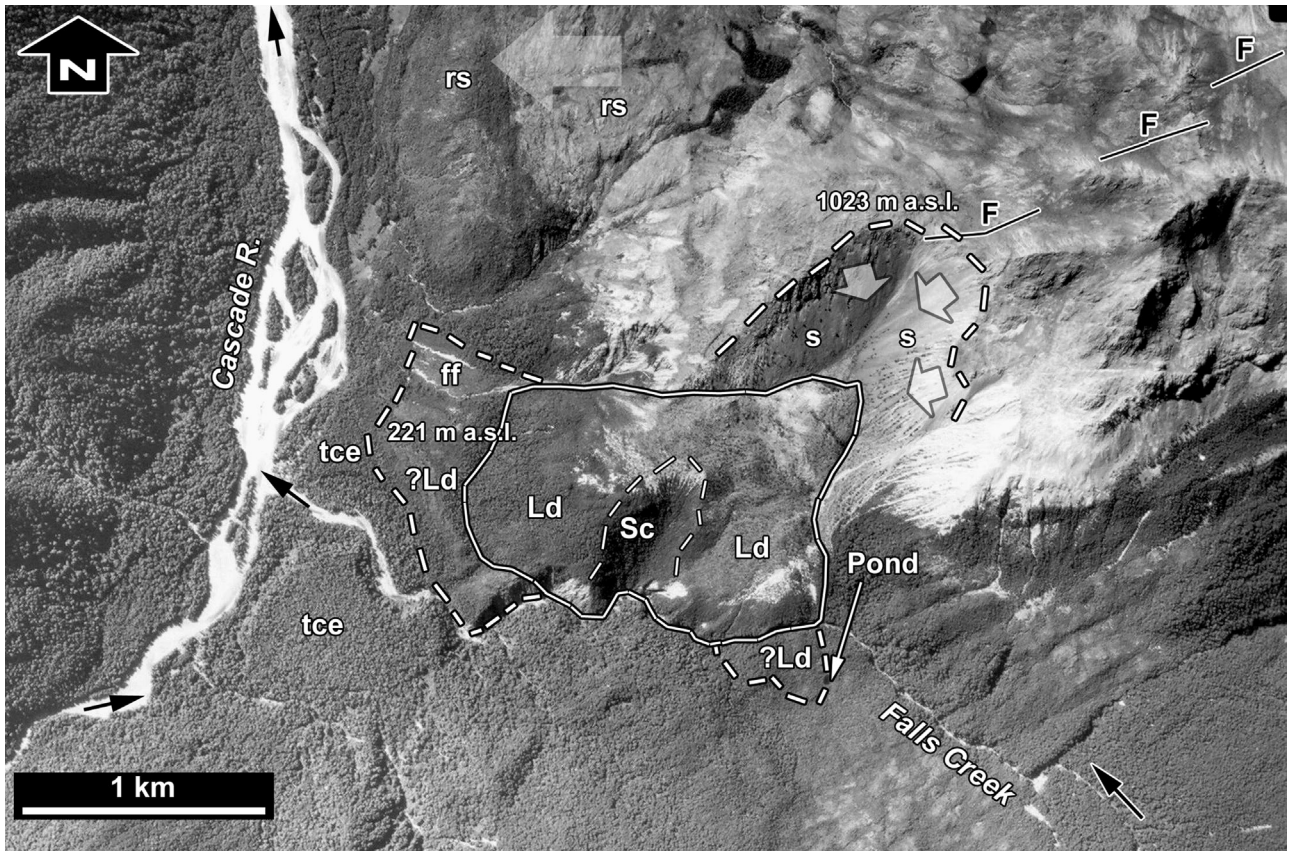

Figure 11. Air photo of large ($V_L \sim 130 \times 10^6$ m^3) deep-seated rotational rockslide on lower Falls Creek, Cascade River (location 21, Figure 1a). Dashed line and white arrows indicate amphitheater-shaped detachment area: s, secondary rockfall scree; Ld, landslide deposit; ?Ld, tentative landslide deposit; Sc, secondary failure scar ($V_L \sim 10 \times 10^6$ m^3); ff, perched debris fan; tce, alluvial fan terrace of Falls Creek; F, fault trace; rs, rock slide (faint white arrow indicates direction of movement). Black arrows indicate flow directions. Scale is approximate. Image is courtesy of Land Information New Zealand, Crown Copyright Reserved (SNC8321/H13).

morphology, and divide spacing. It implies that landslide-triggering earthquakes affect mountain basins not only through forcing channel adjustment to base-level change, but also through catastrophic divide corrections induced by slope-clearing failures.

[28] At the highest length scale of landsliding, giant ($V_L \sim 10^{10}$ m^3) and possibly chronic DSGSD divert low-order drainage and shape local (10^1 to 10^2 m) relief, and form bulging or planar hillslopes [*Whitehouse*, 1986, Figure 14]. Tensional depressions and ridge rents form hanging valleys with elongated flow paths and high sediment storage (Figure 14).

5.2. Large Landslides and Threshold Hillslopes

[29] *Burbank et al.* [1996] argued that strikingly uniform slope histograms across the rapidly uplifting Indus basin, NW Himalaya, indicated frequent landsliding in response to fluvial bedrock incision, with hillslopes being at a critical threshold angle φ_c. Hillslopes at $\varphi > \varphi_c$ would be subject to rapid adjustment by landsliding in order to maintain values $\leq \varphi_c$. *Stark and Stark* [2001] proposed the term asymptotic hillslope, where soil and rock properties would control a hillslope equilibrium gradient, while hillslope sediment flux would be solely driven by rates of fluvial incision. This largely merges concepts of incision- and strength-limitation for slope angles and relief [*Schmidt and Montgomery*, 1995]. However, *Montgomery* [2001] pointed out that normally distributed slope histograms did not warrant the presence of threshold hillslopes, while actual figures of φ_c were difficult to obtain.

[30] Randomly sampled and spaced slope histograms are also very uniform in the WSA despite variations in rates of uplift, erosion, and rock type. In fact, histograms subsume and smooth such disparities. Regionally, most of the smaller landslides occur around the regional $\varphi_{mod} = 39°$ (Figure 8a [*Korup*, 2005c]). Only very young large landslides post-date the DEM data, allowing specification of their prefailure topography. For instance, the 1999 Mount Adams rock avalanche detached from ridge slopes with $\varphi_{mod} = 48°$ ($\Phi = 46° \pm 9°$; Figure 12b). However, this failure was rather shallow, and while no post-failure slope measurements are available, observations suggest similarly steep slopes in the scarp, but lower slopes in the deposit area. However, at the hillslope scale, both failure planes and deposits of many large deep-seated landslides exhibit slopes $< \varphi_{mod}$ at the same length scale of measurement (Table 1 and Figure 12). Conversely, mean hillslope Φ does not contribute to clarify the relationship between large landslides and

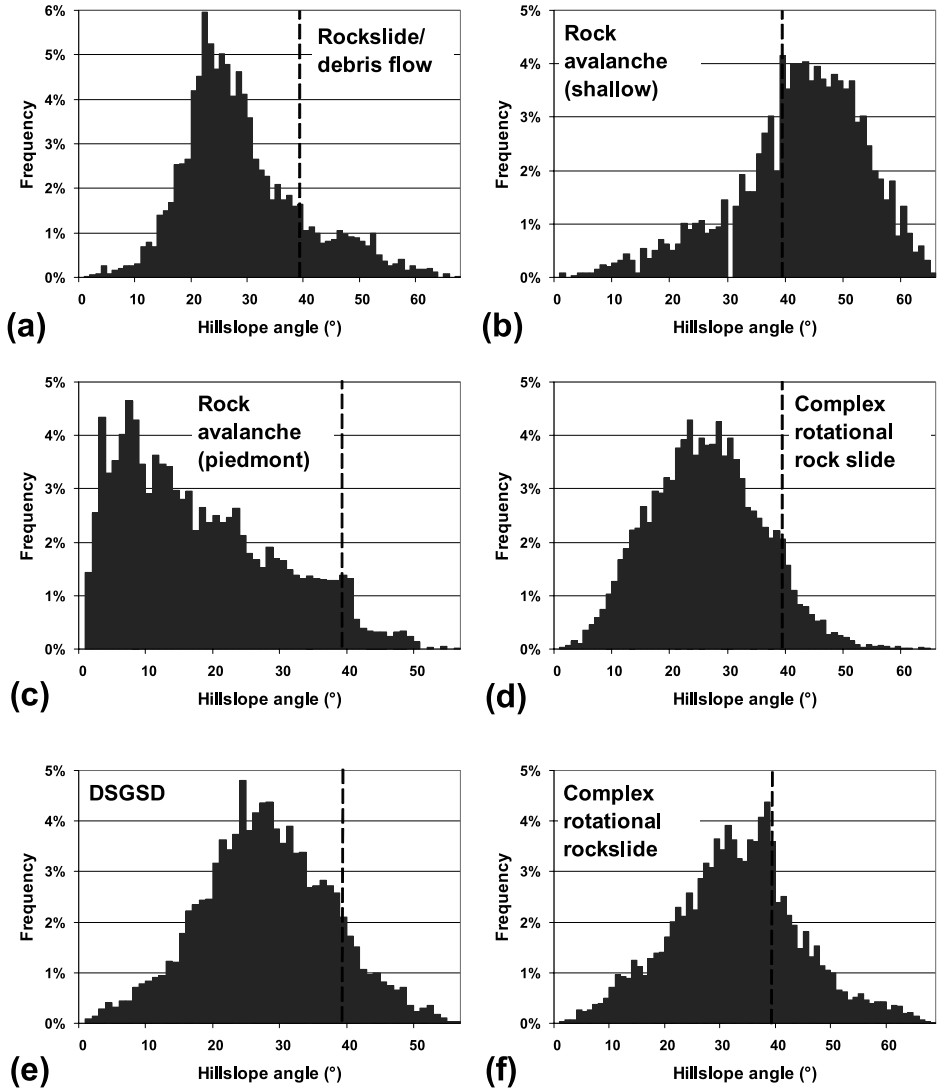

Figure 12. Area-normalized slope histograms derived from a 25-m DEM of large bedrock landslides. (a) Ruera, Copland R. (b) Mount Adams, Poerua R. (c) Selbourne Spur, Waiatoto R. (d) Misty Peak, Karangarua R. (e) Bealy Range, Haast R. (f) Hyperia, Waiatoto R. Dashed lines denote regional modal slope $\varphi_{mod} = 39°$ (all derived at 75-m length scale). Note that shallow failures (Figure 12b) and those with low displacement of rock masses (f) have modes at φ_{mod}.

possible threshold hillslopes (Table 3). Thus, although threshold hillslopes may result from smaller and more numerous landslides (Figure 3), larger events appear to be more persistent forms of hillslope adjustment responding to processes other than slope steepening by fluvial bedrock incision exclusively. Also, many of the large landslides with low displacement (Figure 12f) contradict the notion of rapid slope adjustment to river downcutting. It remains to be tested, whether, for instance, large landslides would preferentially occur along structurally weak portions of the landscape in the WSA, as their spatial correlation to lineaments would suggest.

[31] Giant ($V_L > 10^9$ m^3) landslides may further completely reorganize mountain relief despite local topographic constraints [*Hancox and Perrin*, 1994; *Weidinger et al.*, 2002]. The 27-km^3 Green Lake rockslide-avalanche in the adjacent Fiordland Mountains [*Hancox and Perrin*, 1994], for example, completely reshaped relief over $A_L \sim 55$ km^2, nearly half of which now has $\varphi < 20°$. These subdued slopes result from thick hummocky debris sheets, and perched and partly infilled landslide ponds, occupying the former valley floor. While such giant landslides lower slope relief, their often river-damming deposits enhance local valley-floor relief, before being breached or backfilled with sediment [*Abele*, 1974; *Hewitt*, 2002].

5.3. Implications for Geomorphic Process Response

[32] Slope-area plots offer a better differentiation of the generally lower slopes φ of landslide terrain, while offering a link to geomorphic process regimes. Large landslides lower steepness and concavity indices k_{s*} and θ upstream of the fluvial channelization threshold (Figure 10), where debris flows tend to dominate the geomorphic process regime [*Sklar and Dietrich*, 1998; *Dietrich et al.*, 2003].

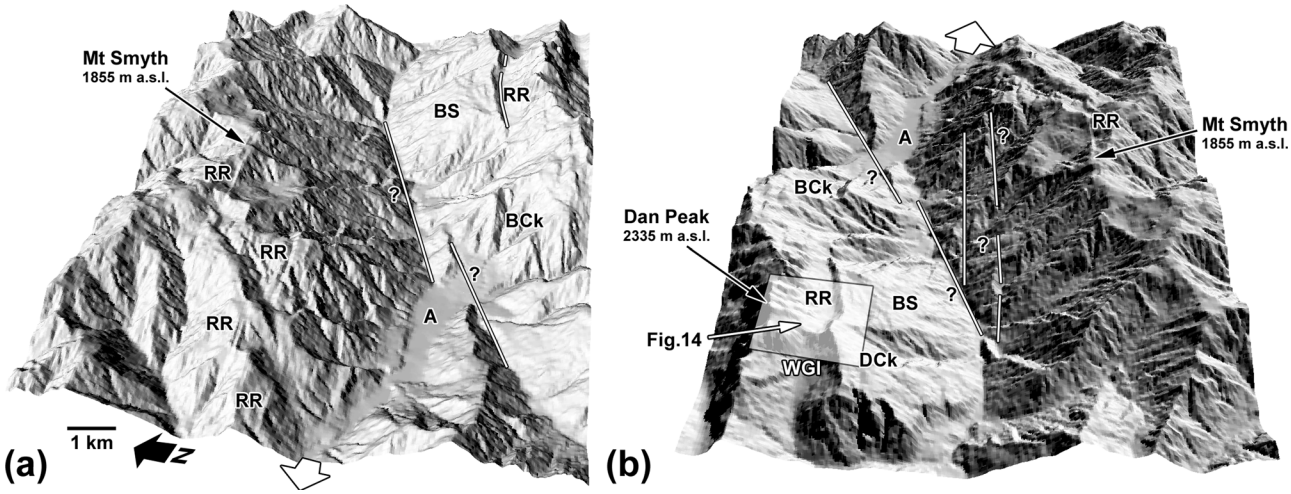

Figure 13. Shaded relief images of deep-seated gravitational slope deformation (DSGSD), Wanganui River (location 2, Figure 1a) between Smyth and Lord Ranges. (a) View from W: RR, ridge rent; A, Adams Flat; BCk, Benighted Creek; BS, bulging rock slope; ?, tentative secondary faults (note stepover). (b) View from E: WGl, Wilberg Glacier; DCk, Devastation Creek. Location of Figure 14 is indicated by rectangle. White arrows indicate flow of Wanganui River.

Lague and Davy [2003] used slope-area relationships in the soil-mantled Siwalik Hills of Nepal to predict long-term hillslope erosion by debris flows. Large and deep-seated landslides in the WSA, however, occupy a length scale encompassing colluvial, debris-flow, and shallow landsliding, as well as fluvial processes (Figure 10). Hence the changes to k_s* and θ due to large landslides provide a means to quantify scatter in slope-area plots, which may otherwise be interpreted as changes in boundary conditions such as uniform rock uplift, steady state topography, homogenous lithology, or constant erosion rates [*Sklar and Dietrich*, 1998]. The effects described here focus on hillslope mor-

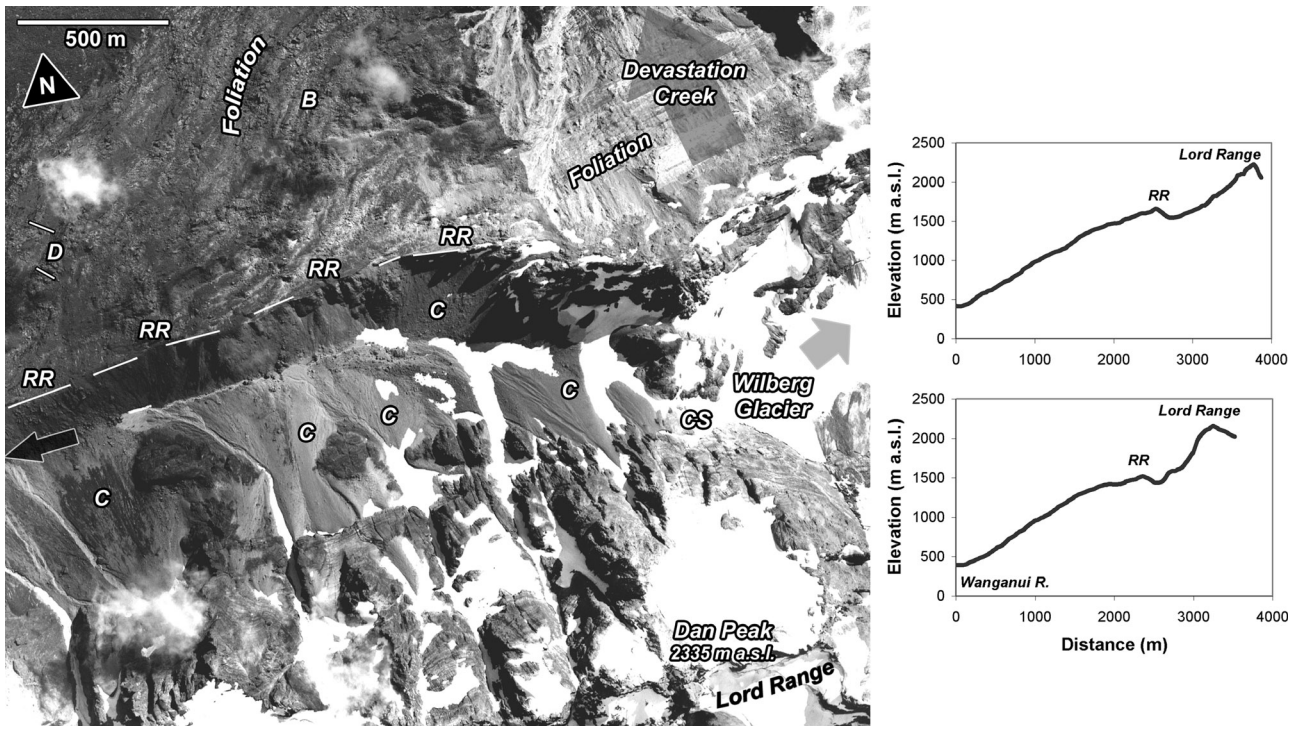

Figure 14. Air photo detail of large ridge rent at Devastation Creek, Wanganui River (for location, see Figure 13). RR, ridge rent (also see N–S trending slope cross sections on right); C, snow avalanche/rockfall/debris flow cones; B, bulging slope (note outwardly convex foliation mimicking contour lines); D, local faulting; CS, Camp Saddle. Image is courtesy of Land Information New Zealand, Crown Copyright Reserved (SNC8341/I37). Arrows indicate flow directions.

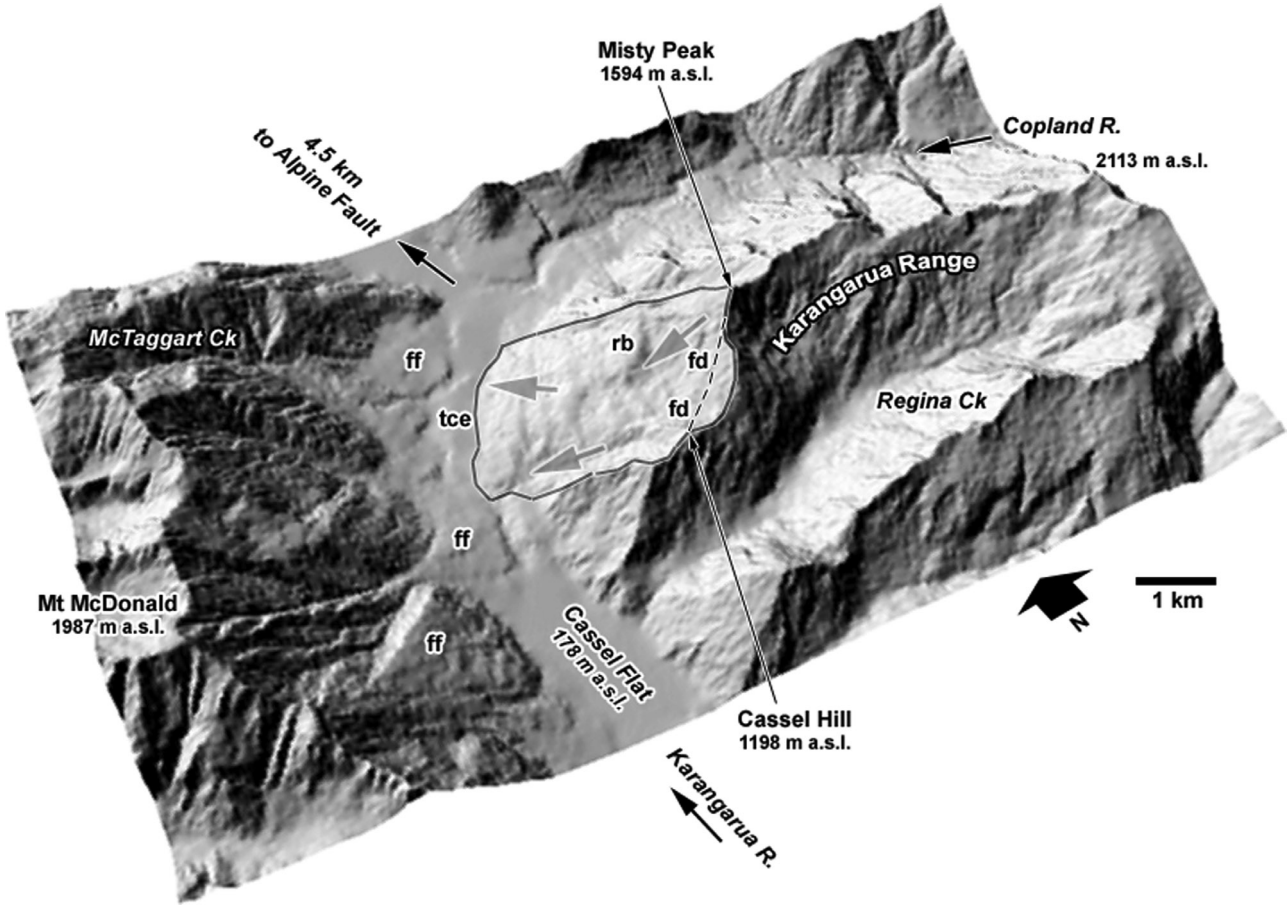

Figure 15. Shaded relief image of Karangarua-Copland River junction (locations 8/9, Figure 1a). Large ($A_L \sim 6.7$ km^2; $V_L \sim 800 \times 10^6$ m^3) prehistoric deep-seated complex rockslide (gray arrows) in the western Karangarua Range below Misty Peak has caused divide retreat by ~0.5 km, headward catchment extension, and stream piracy (fd, former divide; rb, rotated rock block with low-order drainage disruption; tce, fluvial terraces; ff, tributary debris fans). Note that Cassel Flat has formed in the backwater of tributary fan and landslide deposits. Black arrows indicate flow directions.

phology, although large landslides may equally affect the steepness and concavity of river long profiles [*Korup*, 2006].

[33] Other slope-area based predictors such as the SPI are weakly influenced by large landslides (Table 3), since the range and variability of values of SPI may easily smooth out local changes to A_C owing to landslide-induced divide correction. Low sensitivity to landslide effects is also the case for Melton's Ruggedness Number,

$$R_R = H_C A_C^{-0.5}, \tag{5}$$

which was found a reasonable predictor of debris-flow process dominance in small basins in the central Southern Alps [*De Scally and Owens*, 2004]. Even a large landslide such as at Misty Peak (Figure 15) managed to reduce R_R by only <3%, assuming that H_C was unaffected by failure. Arguably, the prediction potential of R_R and similar indices using terrain variables measured at length scales substantially larger than that of large landslides is sensitive enough to capture such changes. Moreover, geomorphic process response to large landslides appears to be much more immediate and significant in terms of catastrophic sediment production and delivery [*Korup et al.*, 2004].

5.4. Implications for Regional Sediment Budgets

[34] Regional inventories find increasing use for quantifying landslide sediment production in mountain belts [*Hovius et al.*, 1997, 2000; *Martin et al.*, 2002; *Brardinoni and Church*, 2004; *Malamud et al.*, 2004], yet very few databases contain large events. *Hovius et al.* [1997] showed that larger failures dominated sediment production from historic landslides ($A_L < 1$ km^2) in the montane zone of the WSA. The volume stored in individual large ($A_L \geq 1$ km^2) landslide deposits (Table 1) is theoretically equal to 10^0–10^2 years of total sediment production from the smaller landslides for a given basin [*Korup*, 2005c], assuming that the magnitude-frequency relationship remains constant over these timescales [*Crozier and Glade*, 1999].

[35] Although the landslide sample presented here complements that of *Hovius et al.* [1997], the lack of absolute ages rules out the quantification of sediment production and delivery rates for large landslides. Thus the long-term contribution of large landslides to the sediment budget

remains unresolved. No data exist on whether fluvial erosion, surface runoff, and secondary failures exploiting large landslide deposits would have higher process rates than on the surrounding hillslopes. However, recurrent secondary toe-slope failures of up to $V_L \sim 10^7$ m^3 are inferred to result from close feedback between landslide motion and fluvial undercutting (Table 1). These observations fit with those of *Gerrard and Gardner* [2000], who argued that large landslides in the Middle Hills of Nepal would dominate hillslope morphology, while setting the stage for smaller ones.

[36] Pulsed and excessive sediment delivery from single large landslides or regional landsliding episodes may similarly contribute significantly to regional sediment flux, but are difficult to distinguish from long-term background rates [e.g., *Pearce and Watson*, 1986; *Korup et al.*, 2004]. *Montgomery and Brandon* [2002] noted a relationship between long-term regional denudation and mean local relief in high mountain belts. The effects of large landslides on local relief in the WSA however cannot be detected sufficiently enough at orogen-scale (10^2 km) to similarly underline their role in sediment production and denudation.

[37] The preservation of landslide deposits storing 10^6–10^{10} m^3 of sediment despite high denudation rates is at odds with the assumptions of *Hovius et al.* [1997] that landslide debris would be exported from the catchments rapidly and without major storage. Even on the simplistic assumption of elevated sediment yields purely derived from landslide debris, many of the deposits would persist for 10^1–10^3 years on average before being fully eroded. Mature forest cover on many large landslide deposits attests to residence times of 10^2 years. This is not to say that all large landslides contribute to long-term sediment storage, especially since the amount of debris that has been eroded can rarely be accounted for [*Korup et al.*, 2004].

5.5. Implications for Models of Hillslope Evolution

[38] Large landslides shape slope morphology and leave imprints that locally may persist for 10^1–10^4 years [*Whitehouse*, 1986]. Hence numerical modeling of mountain landscape evolution concerned with these timescales needs to take account of such processes [e.g., *Stark and Stark*, 2001]. Infinite-slope stability models based on changes in pore water pressure contribute to the predicting of shallow and more frequent events within the landslide spectrum [*Hennrich and Crozier*, 2004], while helping to explain their potential topographic outcome. Modeling of deep-seated failures [e.g., *Densmore et al.*, 1998], however, needs to integrate additional controls to those of climatic forcing, such as triggering by earthquake shaking, undercutting, or gravitational stress release in jointed rock mass. This complexity limits physically based modeling of large landslides to specific sites, whereas regional approaches to deep-seated slope failure and transport laws are rare owing to the lack of sufficient field parameterization [*Dietrich et al.*, 2003]. Thus different types of slope instability may require suitable, yet compatible, approaches to model their effect on mountain relief. The fact that gravitational stress alone, i.e., without any obvious or instantaneous trigger, may initiate DSGSD affecting up to 10^1 km^2 is a pertinent issue not yet addressed in models of landscape evolution. *Molnar* [2004] pointed out that topographically induced stress in areas of high relief may lead to fracturing of intact rock and thus provide means to enhance effective fluvial incision into bedrock. He argued that static fatigue under a topographically induced differential stress could be a rate-limiting process of incision where relief is high, slopes are steep, and bed load transport is rapid.

6. Conclusions

[39] Large and mostly deep-seated landslides have left numerous persistent geomorphic imprints on hillslope morphology in the WSA. These landslides attain kilometer-scale runout, extend over 50% of total basin relief, in 70% are slope-clearing features, and thus are important agents of relief limitation. Geomorphometric analysis demonstrates that at basin scale (10^0–10^1 km), large landslides cause lowering of mean elevation, mean local relief, relief variability, standard deviations of local slope, and modal slope. These differences between landslide-affected and surrounding terrain gradually blend with relief characteristics at orogen scale (10^2 km), thus limiting automated slope-failure detection. Landslide effects inferred from histogram data are spatially better resolved in hillslope- to basin-scale slope-area relationships, where landslides lower the steepness and concavity of hillslopes, thus possibly adding scatter to erosion laws based on such data. Most importantly for analysis and interpretation of DEM data, these geomorphic signatures are the result, rather than the initiating conditions for large landslides.

[40] The detection and quantification of landslide imprints is highly sensitive to the length scales of slope failure, topography, sampling radius, and DEM resolution. At the hillslope scale, visual interpretation of local morphologic contrasts otherwise subsumed by terrain variables or histograms remains essential for DEM-based landslide detection and mapping in densely forested or otherwise inaccessible (e.g., submarine or extraterrestrial) terrain especially [e.g., *Aharonson et al.*, 2001; *McKean and Roering*, 2004]. Mean slope angle, for example, is a measure insensitive to landslide effects in the WSA, and does not elucidate the relationship between large landslides and potential threshold hillslopes in the region. However, large landslides in the WSA have occurred on subcritical slopes, and have formed low-gradient deposits favorable to secondary landslides. Low-displacement failure and creep movement are other inferred characteristics of large landslides in the region not accounted for in concepts of threshold hillslopes.

[41] Qualitative API further confirms that large landslides are important agents of relief limitation and destruction in the WSA. Slope-clearing failures control divide positions, geometrically distort low-order catchments, form hanging valleys, and cause stream piracy. Volumes mobilized and stored by individual landslide deposits are theoretically equal to 10^2 years of basin-wide shallow landsliding. Even at elevated erosion rates, many of the deposits would reside in the landscape for up to 10^3 years, indicating significant sediment storage on hillslopes and some valley floors despite high denudation rates. Geomorphic imprints of large landslides in the WSA are evident and persistent over 10^2–10^4 years. Hence there is a need for refining current models of incision- and strength-limited hillslope adjustment, relief

production and destruction in tectonically active mountain belts, especially since large-scale landsliding may not exclusively respond to fluvial bedrock incision, but rather represent a rate-limiting process in itself. Future work will also need to elucidate whether and how rapidly landslides obliterate fluvial and glacial relief, thus altering morphologic adjustments to tectonic and climatic forcing.

Notation

A_C contributing catchment area.
A_L landslide-affected planform area (scarp and deposit).
A_{LT} total landslide-affected area within a sample.
A_r reference area for normalization of slope-area relationships.
b exponent of the landslide volume-area regression.
E elevation.
$f(A_L)$ spatial density of landsliding.
H_C total basin relief.
H_L height of landslide from scarp to deposit toe.
H_R mean local relief, i.e., maximum elevation difference, within radius R.
H_S local slope relief, i.e., elevation difference between divide and trunk channel.
k_s steepness index.
k_{s*} averaged steepness index for an arbitrarily fixed reference concavity θ.
L_L maximum landslide runout from scarp to toe.
M earthquake magnitude.
n sample number.
r correlation coefficient.
R sampling radius.
R_R Melton's Ruggedness Number.
S local slope gradient.
SD_R relief variability, i.e., standard deviation of elevation within radius R.
SD_φ standard deviation of slope within radius R.
SPI stream power index [*Moore et al.*, 1993].
S_r reference slope for normalization of slope-area relationships.
β slope of landslide frequency density curve.
β' slope of cumulative landslide-area curve.
V_L landslide volume.
ε intercept of the landslide volume-area regression.
θ concavity index.
θ_r reference concavity index.
φ slope angle.
Φ mean slope angle.
φ_c threshold slope angle.
φ_{mod} modal slope angle.
γ estimated mean angle of landslide failure plane.

[42] **Acknowledgments.** Thanks are owed to the support and advice by Mike Crozier, Tim Davies, and Mauri McSaveney. Early parts of this study were funded by a Victoria University of Wellington Scholarship. Alex Densmore and Kelin Whipple are thanked for devoting their time to stimulating discussions. Grant Dellow and Nick Perrin kindly provided some of the landslide location data. Constructive reviews and encouraging comments by Robert S. Anderson, T. C. Hales, Niels Hovius, an anonymous JGR Associate Editor, and a reviewer are greatly appreciated.

References

Abele, G. (1974), Bergstürze in den Alpen – ihre Verbreitung, Morphologie und Folgeerscheinungen, *Wiss. Alpenvereinshefte*, *25*, 247 pp.

Agliardi, F., G. Crosta, and A. Zanchi (2001), Structural constraints on deep-seated slope deformation kinematics, *Eng. Geol.*, *59*, 83–102.

Aharonson, O., M. T. Zuber, and D. H. Rothman (2001), Statistics of Mars' topography from the Mars Orbiter Laser Altimeter: Slopes, correlations, and physical models, *J. Geophys. Res.*, *106*(E10), 23,723–23,735.

Beck, A. C. (1968), Gravity faulting as a mechanism of topographic adjustment, *N. Z. J. Geol. Geophys.*, *11*, 191–199.

Blair, T. C. (1999), Alluvial fan and catchment initiation by rock avalanching, Owens Valley, California, *Geomorphology*, *28*, 201–221.

Brardinoni, F., and M. Church (2004), Representing the landslide magnitude-frequency relation: Capilano River basin, British Columbia, *Earth Surf. Processes Landforms*, *29*, 115–124.

Bull, W. B., and M. T. Brandon (1998), Lichen dating of earthquake-generated regional rock-fall events, Southern Alps, New Zealand, *Geol. Soc. Am. Bull.*, *110*, 60–84.

Burbank, D. W., J. Leland, E. Fielding, R. S. Anderson, N. Brozovic, M. R. Reid, and C. Duncan (1996), Bedrock incision, rock uplift, and threshold hillslopes in the northwestern Himalaya, *Nature*, *379*, 505–510.

Chigira, M. (1992), Long-term gravitational deformation of rocks by rock mass creep, *Eng. Geol.*, *32*, 157–184.

Craw, D., E. Nelson, and P. O. Koons (2004), Structure and topographic evolution of the Main Divide in the Landsborough-Hopkins area of the Southern Alps, New Zealand, *N. Z. J. Geol. Geophys.*, *46*, 553–562.

Crozier, M. J., and T. Glade (1999), Frequency and magnitude of landsliding: Fundamental research issues, *Z. Geomorphol. Suppl.*, *115*, 141–155.

Cruden, D. M., and D. J. Varnes (1996), Landslide types and processes, in *Landslides, Investigation and Mitigation*, edited by A. K. Turner and R. L. Schuster, *Spec. Rep. 247*, pp. 36–75, Transp. Res. Board, Natl. Res. Counc., Washington, D. C.

Dadson, S. J., et al. (2004), Earthquake-triggered increase in sediment delivery from an active mountain belt, *Geology*, *32*, 733–736.

Densmore, A. L., and N. Hovius (2000), Topographic fingerprint of bedrock landslides, *Geology*, *28*, 371–374.

Densmore, A. L., R. S. Anderson, B. G. McAdoo, and M. A. Ellis (1997), Hillslope evolution by bedrock landslides, *Science*, *275*, 369–372.

Densmore, A. L., M. A. Ellis, and R. S. Anderson (1998), Landsliding and the evolution of normal-fault-bounded mountains, *J. Geophys. Res.*, *103*(B7), 15,203–15,219.

De Scally, F. A., and I. F. Owens (2004), Morphometric controls and geomorphic responses on fans in the Southern Alps, New Zealand, *Earth Surf. Processes Landforms*, *29*, 311–322.

Dietrich, W. E., D. Bellugi, L. S. Sklar, J. D. Stock, A. M. Heimsath, and J. J. Roering (2003), Geomorphic transport laws for predicting landscape form and dynamics, in *Prediction in Geomorphology*, *Geophys. Monogr. Ser.*, vol. 135, edited by R. M. Iverson and P. Wilcock, pp. 103–132, AGU, Washington, D. C.

Duvall, A., E. Kirby, and D. Burbank (2004), Tectonic and lithologic controls on bedrock channel profiles and processes in coastal California, *J. Geophys. Res.*, *109*, F03002, doi:10.1029/2003JF000086.

Finlayson, D. P., and D. R. Montgomery (2003), Modeling large-scale fluvial erosion in geographic information systems, *Geomorphology*, *53*, 147–164.

Fort, M. (2000), Glaciers and mass wasting processes: Their influence on the shaping of the Kali Gandaki Valley (higher Himalaya of Nepal), *Quat. Int.*, *65/66*, 101–119.

Fort, M., and J. P. Peulvast (1995), Catastrophic mass-movements and morphogenesis in the peri-Tibetan ranges: Examples from West Kunlun, East Pamir and Ladakh, in *Steepland Geomorphology*, edited by O. Slaymaker, pp. 171–198, John Wiley, Hoboken, N. J.

Gerrard, A. J., and R. A. M. Gardner (2000), The role of landsliding in shaping the landscape of the Middle Hills, Nepal, *Z. Geomorphol. Suppl. Band*, *122*, 47–62.

Hancox, G. T., and N. D. Perrin (1994), Green Lake Landslide: A very large ancient rock slide in Fiordland, New Zealand, in *Proceedings of the 7th International Congress International Association of Engineering Geology*, edited by R. Oliveira et al., pp. 1677–1689, A. A. Balkema, Brookfield, Vt.

Hanson, C. R., R. J. Norris, and A. F. Cooper (1990), Regional fracture patterns east of the Alpine Fault between the Fox and Franz Josef Glaciers, Westland, New Zealand, *N. Z. J. Geol. Geophys.*, *33*, 617–622.

Henderson, R. D., and S. M. Thompson (1999), Extreme rainfalls in the Southern Alps of New Zealand, *J. Hydrol. N. Z.*, *38*, 309–330.

Hennrich, K., and M. J. Crozier (2004), A hillslope hydrology approach for catchment-scale slope stability analysis, *Earth Surf. Processes Landforms*, *29*, 599–610.

Hermanns, R. L., and M. R. Strecker (1999), Structural and lithological controls on large Quaternary rock avalanches (sturzstroms) in arid northwestern Argentina, *Geol. Soc. Am. Bull.*, *111*, 934–948.

Hewitt, K. (2002), Postglacial landform and sediment associations in a landslide-fragmented river system: The Transhimalayan Indus streams, Central Asia, in *Landscapes of Transition. Landform Assemblages and Transformations in Cold Regions*, edited by K. Hewitt et al., pp. 63–91, Springer, New York.

Hicks, M., U. Shankar, and A. McKerchar (2003), Sediment yield estimates: A GIS tool, *Water Atmos.*, *11*, 26–27.

Hovius, N., C. P. Stark, and P. A. Allen (1997), Sediment flux from a mountain belt derived from landslide mapping, *Geology*, *25*, 231–234.

Hovius, N., C. P. Stark, M. A. Tutton, and L. D. Abbott (1998), Landslide-driven drainage network evolution in a pre-steady-state mountain belt: Finisterre Mountains, Papua New Guinea, *Geology*, *26*, 1071–1074.

Hovius, N., C. P. Stark, H. T. Chu, and J. C. Lin (2000), Supply and removal of sediment in a landslide-dominated mountain belt: Central Range, Taiwan, *J. Geol.*, *108*, 73–89.

Kirby, E., K. X. Whipple, W. Tang, and Z. Chen (2003), Distribution of active rock uplift along the eastern margin of the Tibetan Plateau: Inferences from bedrock channel longitudinal profiles, *J. Geophys. Res.*, *108*(B4), 2217, doi:10.1029/2001JB000861.

Korup, O. (2004), Geomorphic implications of fault zone weakening: Slope instability along the Alpine Fault, South Westland to Fiordland, *N. Z. J. Geol. Geophys.*, *47*, 257–267.

Korup, O. (2005a), Large landslides and their effect on sediment flux in South Westland, New Zealand, *Earth Surf. Processes Landforms*, *30*, 305–323.

Korup, O. (2005b), Geomorphic imprint of mass movements on alpine river systems, southwest New Zealand, *Earth Surf. Processes Landforms*, *30*, 783–800.

Korup, O. (2005c), Distribution of landslides in southwest New Zealand, *Landslides*, *2*, 43–51.

Korup, O. (2006), Rock-slope failure and the river long profile, *Geology*, *34*, 45–48.

Korup, O., and M. Crozier (2002), Landslide types and geomorphic impact on river channels, Southern Alps, New Zealand, in *Landslides: Proceedings of the 1st European Conference on Landslides 24–26 June 2002, Prague*, edited by J. Rybar, J. Stemberk, and P. Wagner, pp. 233–238, A. A. Balkema, Brookfield, Vt.

Korup, O., M. J. McSaveney, and T. R. H. Davies (2004), Sediment generation and delivery from large historic landslides in the Southern Alps, New Zealand, *Geomorphology*, *61*, 189–207.

Lague, D., and P. Davy (2003), Constraints on the long-term colluvial erosion law by analyzing slope-area relationships at various tectonic uplift rates in the Siwaliks Hills (Nepal), *J. Geophys. Res.*, *108*(B2), 2129, doi:10.1029/2002JB001893.

Malamud, B. D., D. L. Turcotte, F. Guzzetti, and P. Reichenbach (2004), Landslide inventories and their statistical properties, *Earth Surf. Processes Landforms*, *29*, 687–711.

Martin, Y., K. Rood, J. W. Schwab, and M. Church (2002), Sediment transfer by shallow landsliding in the Queen Charlotte Islands, British Columbia, *Can. J. Earth Sci.*, *39*, 189–205.

McKean, J., and J. Roering (2004), Objective landslide detection and surface morphology mapping using high-resolution airborne laser altimetry, *Geomorphology*, *57*, 331–351.

McSaveney, M. J. (2002), Recent rockfalls and rock avalanches in Mount Cook National Park, New Zealand, in *Catastrophic Landslides: Effects, Occurrence, and Mechanisms*, *Rev. Eng. Geol.*, vol. XV, edited by S. G. Evans and J. V. DeGraff, pp. 35–70, Geol. Soc. of Am., Boulder, Colo.

Molnar, P. (2004), Interactions among topographically induced elastic stress, static fatigue, and valley incision, *J. Geophys. Res.*, *109*, F02010, doi:10.1029/2003JF000097.

Montgomery, D. R. (2001), Slope distributions, thresholds hillslopes, and steady-state topography, *Am. J. Sci.*, *301*, 432–452.

Montgomery, D. R., and M. T. Brandon (2002), Topographic controls on erosion rates in tectonically active mountain ranges, *Earth Planet. Sci. Lett.*, *201*, 481–489.

Moore, I. D., A. K. Turner, J. P. Wilson, S. K. Jenson, and I. E. Band (1993), GIS and land-surface–subsurface modeling, in *Environmental Modelling with GIS*, edited by M. F. Goodchild, B. O. Parks, and L. T. Steyaert, pp. 213–230, Oxford Univ. Press, New York.

Norris, R. J., and A. F. Cooper (2000), Late Quaternary slip rates and slip partitioning on the Alpine Fault, New Zealand, *J. Struct. Geol.*, *23*, 507–520.

Pearce, A. J., and A. J. Watson (1986), Effects of earthquake-induced landslides on sediment budget and transport over a 50-yr period, *Geology*, *14*, 52–55.

Schmidt, K. M., and D. R. Montgomery (1995), Limits to relief, *Science*, *270*, 617–620.

Shang, Y., Z. Yang, L. Li, D. Liu, Q. Liao, and Y. Wang (2003), A super-large landslide in Tibet in 2000: Background, occurrence, disaster, and origin, *Geomorphology*, *54*, 225–243.

Shroder, J. F., Jr. (1998), Slope failure and denudation in the western Himalaya, *Geomorphology*, *26*, 81–105.

Sklar, L., and W. E. Dietrich (1998), River longitudinal profiles and bedrock incision models: Stream power and the influence of sediment supply, in *Rivers Over Rocks: Fluvial Processes in Bedrock Channels*, *Geophys. Monogr. Ser.*, vol. 107, edited by K. J. Tinkler and E. E. Wohl, pp. 237–260, AGU, Washington, D. C.

Snyder, N. P., K. X. Whipple, G. E. Tucker, and D. J. Merritts (2003), Channel response to tectonic forcing: Field analysis of stream morphology and hydrology in the Mendocino triple junction region, northern California, *Geomorphology*, *53*, 97–127.

Soeters, R., and C. J. van Westen (1996), Slope instability recognition, analysis, and zonation, in *Landslides: Investigation and Mitigation*, edited by A. K. Turner and R. L. Schuster, *Spec. Rep. 247*, pp. 129–177, Transp. Res. Board, Natl. Res. Counc., Washington, D. C.

Stark, C. P., and G. J. Stark (2001), A channelization model of landscape evolution, *Am. J. Sci.*, *301*, 486–512.

Strom, A. L. (1998), Giant ancient rock slides and rock avalanches in the Tien Shan Mountains, Kyrgyzstan, *Landslide News*, *11*, 20–23.

Tippett, J. M., and P. J. J. Kamp (1995), Quantitative relationships between uplift and relief parameters for the Southern Alps, New Zealand, as determined by fission track analysis, *Earth Surf. Processes Landforms*, *20*, 153–175.

Weidinger, J. T., J. M. Schramm, and F. Nuschej (2002), Ore mineralization causing slope failure in a high-altitude mountain crest—On the collapse of an 8000 m peak in Nepal, *J. Asian Earth Sci.*, *21*, 295–306.

Wells, A., M. D. Yetton, R. F. Duncan, and G. H. Stewart (1999), Prehistoric dates of the most recent Alpine Fault earthquakes, New Zealand, *Geology*, *27*, 995–998.

Whipple, K. X. (2004), Bedrock rivers and the geomorphology of active orogens, *Annu. Rev. Earth Planet. Sci.*, *32*, 151–185.

Whipple, K. X., and G. E. Tucker (2002), Implications of sediment-flux-dependent river incision models for landscape evolution, *J. Geophys. Res.*, *107*(B2), 2039, doi:10.1029/2000JB000044.

Whitehouse, I. E. (1983), Distribution of large rock avalanche deposits in the central Southern Alps, New Zealand, *N. Z. J. Geol. Geophys.*, *26*, 272–279.

Whitehouse, I. E. (1986), Geomorphology of a compressional plate boundary, Southern Alps, New Zealand, in *International Geomorphology*, edited by V. Gardiner, pp. 897–924, John Wiley, Hoboken, N. J.

O. Korup, WSL Swiss Federal Institute for Snow and Avalanche Research SLF, CH–7260 Davos, Switzerland. (korup@slf.ch)